

Learning Structure-from-Motion with Graph Attention Networks

Lucas Brynte

José Pedro Iglesias

Carl Olsson

Fredrik Kahl

Chalmers University of Technology

{brynte, jose.iglesias, caols, fredrik.kahl}@chalmers.se

Abstract

In this paper we tackle the problem of learning Structure-from-Motion (SfM) through the use of graph attention networks. SfM is a classic computer vision problem that is solved through iterative minimization of reprojection errors, referred to as Bundle Adjustment (BA), starting from a good initialization. In order to obtain a good enough initialization to BA, conventional methods rely on a sequence of sub-problems (such as pairwise pose estimation, pose averaging or triangulation) which provide an initial solution that can then be refined using BA. In this work we replace these sub-problems by learning a model that takes as input the 2D keypoints detected across multiple views, and outputs the corresponding camera poses and 3D keypoint coordinates. Our model takes advantage of graph neural networks to learn SfM-specific primitives, and we show that it can be used for fast inference of the reconstruction for new and unseen sequences. The experimental results show that the proposed model outperforms competing learning-based methods, and challenges COLMAP while having lower runtime. Our code is available at: <https://github.com/lucasbrynte/gasfm/>.

1. Introduction

Structure-from-Motion (SfM) is a classic and still relevant problem in computer vision. The goal of SfM is to estimate camera poses and 3D coordinates of keypoints detected across multiple images, and can be formulated as an optimization over m camera matrices $\{\mathbf{P}_i\}$, $i = 1, \dots, m$ and n 3D points $\{\mathbf{X}_j\}$, $j = 1, \dots, n$ of the form

$$\begin{aligned} & \underset{\{\mathbf{P}_i\}, \{\mathbf{X}_j\}}{\text{minimize}} && \sum_{ij} r(\mathbf{m}_{ij}, \mathbf{z}_{ij}) \\ & \text{subject to} && \mathbf{z}_{ij} = \mathbf{P}_i \bar{\mathbf{X}}_j, \forall i, j \end{aligned} \quad (1)$$

where \mathbf{m}_{ij} holds the 2D coordinates of the j^{th} keypoint in the i^{th} image. The loss in (1) is generally chosen as the reprojection error

$$r(\mathbf{m}_{ij}, \mathbf{z}_{ij}) = \|\mathbf{m}_{ij} - \Pi(\mathbf{z}_{ij})\|^2 \quad (2)$$

where $\Pi(\mathbf{x}) = \begin{pmatrix} x_1 & x_2 \\ x_3 & x_3 \end{pmatrix}$, and the nonlinear least squares problem (1), referred to as Bundle Adjustment (BA) [15], can be solved iteratively using second-order methods like Levenberg-Marquardt [15, 41]. Given the sparsity of the problem, sparse computation methods [27] can be used in order to increase the efficiency of the optimization, allowing BA to be used even for scenes with a large number of views or points. However, it is widely known that BA is highly non-convex and tends to converge to the nearest local minimum when not initialized close to the globally optimal solution. As a consequence, BA is typically the last step of a reconstruction pipeline, preceding global SfM methods such as [9, 10, 20, 25], or incremental SfM methods such as [2, 37, 38] that solve a sequence of sub-problems like pairwise pose estimation, pose averaging, triangulation or camera resection [13, 15, 22, 32]. A different approach consists of projective factorization methods [8, 17, 18, 28, 39, 48] which factorize the $2m \times n$ measurement matrix into two rank four matrices corresponding to the camera matrices and 3D points (in homogeneous coordinates). In particular, works like [17, 18, 48] allow initialization-free SfM given their wide basin of convergence, meaning that their methods can be initialized with random camera poses and still converge with a high rate of success to the desired global minimum. Even though these methods have been improving in terms of accuracy and robustness to missing data, factorization-based methods require the input data to be almost completely free of outliers which unfortunately cannot be guaranteed in most real world sequences or datasets, and hence severely compromises the usability of these methods.

A common challenge with all these approaches to solve SfM is their scalability as the number of views and keypoints increase. Incremental SfM tries to tackle this issue by starting with a subset of the views, estimate its reconstruction and incrementally adding more views. Some factorization-based methods can also take advantage of the same sparse computation methods used in BA, which significantly improves their ability to scale with sequence size. While this allows to reconstruct scenes with thousands of views and millions of points, it can still take hours to recover the reconstruction of a single scene.

More recently, deep learning methods for 3D reconstruction and SfM have been proposed [7, 29, 31, 35, 44–47]. Given their increased complexity, these models are able to learn complex relations between the input data, outperforming conventional methods and achieving state-of-the-art results in 3D reconstruction and novel view synthesis when the camera pose and calibration are known [7, 29, 46]. Works such as [31, 46, 47] tackle SfM with deep learning models which different degrees of success.

In DeepSfM [46] the authors propose an end-to-end approach to estimate camera pose and a dense depth map of a target view from multiple source views. Their method estimates a feature map for each of the source views, which are then combined with the feature map of the target view in order to estimate pose and depth cost volumes. These cost volumes are then fed to two heads that estimate the camera pose and depth map of the target view. In PoseDiffusion [44], a probabilistic diffusion framework is proposed to mirror the iterations of bundle adjustment, allowing it to incorporate geometric priors into the problem. The model is trained on object-centric scenes and it is shown that it can generalize to unseen scenes without further training.

In [31], which is the closest work to ours, the authors have pursued an approach similar to projective factorization, taking as input the 2D keypoints tracked along multiple views. These 2D point tracks are processed by a number of linear permutation-equivariant layers, i.e. layers such that a permutation on the rows and/or columns of the input tensor results in the same permutation on the output. The output of these layers is then fed to camera pose and 3D points coordinate regression heads. The model is learned using reprojection errors as loss combined with a hinge loss term to push points in front of the cameras. By using Adam [26] as optimizer along with gradient normalization, the authors show that their method has improved convergence properties compared to random initializations.

A major benefit of learning-based methods is their potential in generalizing to new data after being trained. This can be particularly beneficial to SfM problems since occlusions and missing measurements are common issues that make some scenes particularly challenging to reconstruct. In these cases, the learned model can act as a prior and help constrain the solution based on the data seen during training. However, most of the learning-based methods mentioned for 3D reconstruction or SfM require scene-specific optimization or training, which turns out to be particularly slow for large sequences. PoseDiffusion [44] achieves some degree of generalization to unseen scenes, but it is conditional on the categories and object-centric datasets seen during training. In [31] the authors actually show that their model can be trained on a large collection of scenes and then used for inference on unobserved scenes. However, without fine-tuning on these new scenes (which is

time-consuming) the model’s accuracy is significantly reduced.

In this paper we propose a graph attention network for initialization-free Structure-from-Motion that can be trained on multiple scenes and used for fast inference on new, unseen scenes. Similarly to [31], our network takes as input sparse measured image points, matched across multiple viewpoints, which are processed through a sequence of permutation-equivariant graph cross attention layers. The output of the graph cross attention layers is then processed by two regression heads, one for the 3D points and another for the camera poses. By using graph attention layers instead of linear equivariant maps as in [31], our model is able to better learn the implicit geometric primitives of SfM in the input data, leading to more expressiveness and better generalization to unseen sequences. Additionally, by not requiring time-consuming fine-tuning on unseen scenes, our model is able to provide fast inference, which can then be refined directly with BA with good convergence.

The contributions of the paper can be summarized as:

- We propose graph attention networks for initialization-free Structure-from-Motion that estimates camera parameters and 3D coordinates of 2D keypoints tracked across multiple views;
- The method takes advantage of the graph cross-attention layers, which are equivariant to permutation on the input data regarding order of views and points. We show that these layers can model more complex relations between input data and when combined with data augmentation result in significantly improved performance when compared to baseline methods;
- We evaluate the proposed learned method on unobserved scenes and show that it outperforms competing state-of-the-art learning methods at inference in terms of accuracy without the need of scene-specific model fine-tuning;
- We show that our method achieves competitive results when compared to state-of-the-art conventional Structure-from-Motion pipelines while having a significantly lower runtime.

2. Graph Attention Network Preliminaries

Before introducing our proposed method, we will here briefly outline the graph attention networks that will be utilized – the GATv2 model [4] based on [43].

The GATv2 model is a type of graph neural network (GNN) that carries out aggregation from neighboring nodes with a dynamic attention-based weighted average. The input to a GATv2 layer is a set of current node features $\{\mathbf{h}_i \in \mathbb{R}^d \mid i \in \mathcal{V}\}$ along with a set of directed edges \mathcal{E} defining the graph connectivity. The layer outputs a new set of node features $\{\mathbf{h}'_i \in \mathbb{R}^{d'} \mid i \in \mathcal{V}\}$, by applying a single shared learned function on every node h_i together with its neighbor-

hood $\mathcal{N}_i = \{j \in \mathcal{V} \mid (j, i) \in \mathcal{E}\}$.

First, a scoring function $e : \mathbb{R}^d \times \mathbb{R}^d \rightarrow \mathbb{R}$ is applied on all edges, by feeding the respective source and target node features as input to a shared 2-layer Multi-Layer Perceptron (MLP):

$$e(\mathbf{h}_i, \mathbf{h}_j) = \mathbf{a}^\top \cdot \text{LeakyReLU}(\mathbf{W}[\mathbf{h}_i \parallel \mathbf{h}_j]), \quad (3)$$

where $\mathbf{a} \in \mathbb{R}^d$ and $\mathbf{W} \in \mathbb{R}^{d' \times 2d}$ are learned parameters, and \parallel denotes vector concatenation. The attention scores are then normalized across all neighbors:

$$\alpha_{ij} = \text{softmax}_j(e(\mathbf{h}_i, \mathbf{h}_j)) = \frac{\exp(e(\mathbf{h}_i, \mathbf{h}_j))}{\sum_{j' \in \mathcal{N}_i} \exp(e(\mathbf{h}_i, \mathbf{h}_{j'}))}, \quad (4)$$

and the layer is completed by carrying out a weighted average of linear projections of all source node features:

$$\mathbf{h}'_i = \sum_{j \in \mathcal{N}_i} \alpha_{ij} \cdot \mathbf{W} \mathbf{h}_j. \quad (5)$$

3. Method

We apply a graph attention network model to perform Structure-from-Motion on a desired scene based on its measured image point correspondences. The model then outputs a reconstruction, represented by all m camera matrices and all n scene points. Structure-from-Motion is in general a large and complex optimization problem, and it is not trivially addressed as a learning problem. Our architecture combines the power and expressivity of the attention mechanism, and exploits its inherent permutation equivariance in a meaningful way, while balancing expressivity with efficiency, resulting in a very limited computational and memory footprint considering the task at hand.

The input data for a particular scene consists of a sparse set of measured image point correspondences (point tracks). To represent this data, we define a binary observability matrix $\mathbf{O} \in \{0, 1\}^{m \times n}$, where m is the number of views and n is the number of scene points, and where $\mathbf{O}_{ij} = 1$ if and only if scene point j is observed in image i . Furthermore, let $\mathcal{P} = \{\mathbf{m}_{ij} \in \mathbb{R}^2 \mid \mathbf{O}_{ij} = 1\}$ be the collection of observed image point tracks, where \mathbf{m}_{ij} is the (normalized) measured image point for the projection of scene point j in camera i .

3.1. Graph Attention Network Architecture

In this section, we will outline our graph attention network architecture, starting by introducing our feature representation. Then we proceed to define update operations for different feature types, and finally define the entire network architecture based on these operations.

Feature representation. Throughout the network architecture, we maintain and continuously update a set of features of various types¹:

¹For simplicity, we use a slight abuse of set notation here. If there are feature vector duplicates, they are still considered as separate elements.

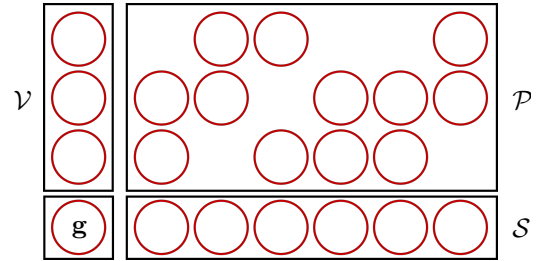


Figure 1. Illustration of the different types of features in the network architecture, for $m = 3$ cameras and $n = 6$ scene points. The projection features \mathcal{P} are represented by a sparse vector-valued matrix, with its sparsity pattern determined by the point track measurements, while view features \mathcal{V} and scene point features \mathcal{S} are represented by dense vector-valued column and row vectors. A single vector \mathbf{g} holds global features.

- *Projection features*, $\mathcal{P} = \{\mathbf{p}_{ij} \in \mathbb{R}^{d_p} \mid \mathbf{O}_{ij} = 1\}$.
- *View features*, $\mathcal{V} = \{\mathbf{v}_i \in \mathbb{R}^{d_v} \mid i = 1, 2, \dots, m\}$.
- *Scene point features*, $\mathcal{S} = \{\mathbf{s}_j \in \mathbb{R}^{d_s} \mid j = 1, 2, \dots, n\}$.
- *Global features*, $\mathbf{g} \in \mathbb{R}^{d_g}$.

The *projection features* \mathbf{p}_{ij} are feature vectors specific to every observed image point. In practice, these are bundled together and organized in a sparse vector-valued matrix, as illustrated by the large top-right matrix in Figure 1. The sparsity pattern of \mathcal{P} will be fixed throughout the network and is determined by \mathbf{O} , which however depends on the scene. The *view features* \mathcal{V} and *scene point features* \mathcal{S} , on their part, are organized in dense vector-valued column and row vectors, respectively, also illustrated in Figure 1. Finally, the *global features* \mathbf{g} , consist of a single globally shared feature vector, and is illustrated in the bottom-left corner of Figure 1.

In order to define graph operations, we see every feature vector as being associated with a corresponding graph node. At this point, note that a simple approach would be to connect all nodes \mathcal{P} , \mathcal{V} , \mathcal{S} , and $\{\mathbf{g}\}$ in one unified graph, and directly apply a graph neural network with global weight sharing. Instead, since the nodes are semantically different, we consider these semantics when choosing the level of weight sharing, and even vary the feature dimension depending on the type of node. In practice, we construct different graphs for propagation between different types of nodes.

Having defined the different feature types, we proceed to define corresponding update operations, which are repeatedly carried out throughout the network. In all pseudo-code, ReLU denotes to the rectified linear unit and LN denotes layer normalization [3]. Linear denotes a learned affine layer and FFN denotes a number of stacked Linear layers interleaved with ReLU activations. Subscripts may occur to emphasize feature dimensions. Note that all of these operations may be applied on multiple nodes at once, with shared parameters. The $+$ notation implies node-wise addition.

Graph Cross-Attention. Procedure 1 is utilized for all feature aggregations throughout the network. It carries out cross-attention [42], attending to and propagating information from one set of input / source nodes \mathcal{H}_1 to another set of output / target nodes $\hat{\mathcal{H}}_2$. The previous target node features \mathcal{H}_2 , if provided, will act as query features when computing attention scores. In the first few layers these may not be available, and initial zero-features are used instead.

In our context, the source nodes and target nodes correspond to different feature types, possibly with different feature dimension. As the source and target nodes are disjoint, we may represent the connectivity by a directed bipartite graph. Furthermore, in our context this graph will often consist of a number of disconnected subgraphs. Procedure 1 essentially acts as a wrapper around a GATv2 layer [4] (for which we use the PyTorch Geometric [11] implementation), while carrying out input normalization, and feature projections as necessary. We consistently use 4 attention heads for the GATv2 layers.

Procedure 1 GRAPHCROSSATTENTION

Input: \mathcal{H}_1 Source node features.
Input: \mathcal{H}_2 Previous target node features (optional).
Input: $\mathcal{E}_{\mathcal{H}_1 \rightarrow \mathcal{H}_2}$ Set of edges from $\mathcal{H}_1 \rightarrow \mathcal{H}_2$.
Input: d_1 Source node feature dimension.
Input: d_2 Target node feature dimension.
Output: $\hat{\mathcal{H}}_2$ Updated target node features.

- 1: $\hat{\mathcal{H}}_1 \leftarrow \text{ReLU}(\text{LN}(\mathcal{H}_1))$
- 2: **if** \mathcal{H}_2 provided **then**
- 3: $\hat{\mathcal{H}}_2 \leftarrow \text{ReLU}(\text{LN}(\mathcal{H}_2))$
- 4: **if** $d_1 \neq d_2$ **then**
- 5: $\hat{\mathcal{H}}_2 \leftarrow \text{Linear}_{d_2 \rightarrow d_1}(\hat{\mathcal{H}}_2)$
- 6: **else**
- 7: $\hat{\mathcal{H}}_2 \leftarrow$ zero features $\vec{0} \in \mathbb{R}^{d_1}$
- 8: $\hat{\mathcal{H}}_2 \leftarrow \text{GATv2Conv}(\hat{\mathcal{H}}_1, \hat{\mathcal{H}}_2, \mathcal{E}_{\mathcal{H}_1 \rightarrow \mathcal{H}_2})$
- 9: **if** $d_1 \neq d_2$ **then**
- 10: $\hat{\mathcal{H}}_2 \leftarrow \text{Linear}_{d_1 \rightarrow d_2}(\hat{\mathcal{H}}_2)$

View & Scene Point Feature Update. View features and scene point features are updated by Procedure 2 and 3, respectively, entirely symmetrical to one another. A directed bipartite graph is constructed by taking \mathcal{P} as source nodes, and \mathcal{V} (or \mathcal{S}) as target nodes, and connecting every projection node with its corresponding view (or scene point) node, corresponding to rows (or columns) of \mathcal{P} . Graph cross-attention according to Procedure 1 is then carried out on the graph, and used as a residual mapping. This is followed by another residual mapping with a feed-forward network. Illustrations of these update operations are provided in Figures 2 and 3.

Global Feature Update. The global feature update, outlined in Procedure 4 is carried out in almost the same manner, but now aggregating from all view features \mathcal{V} and scene point features \mathcal{S} instead of \mathcal{P} . This is carried

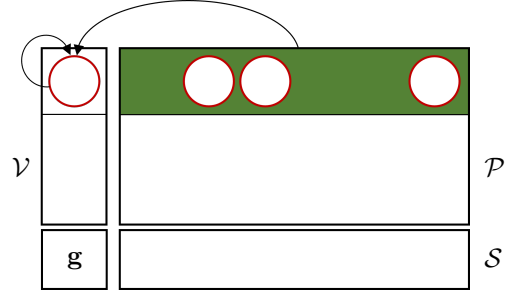


Figure 2. Illustration of the update of a single view feature. All \mathcal{V} features are updated based on their previous value and the corresponding rows of \mathcal{P} .

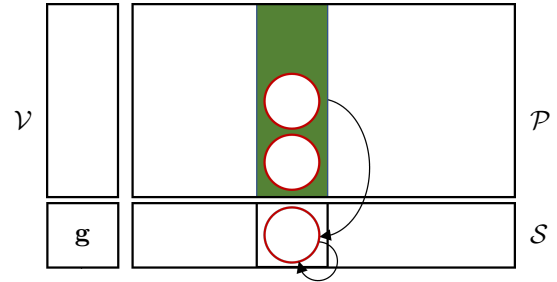


Figure 3. Illustration of the update of a single scene point feature. All \mathcal{S} features are updated based on their previous value and the corresponding columns of \mathcal{P} .

Procedure 2 UPDATEVIEWFEAT

Input: \mathcal{P}, \mathbf{O} Projection features + observability matrix.
Input: \mathcal{V} Previous view features (optional).
Input: d_p, d_v Feature dimensions.
Output: $\hat{\mathcal{V}}$ Updated view features.

- 1: $\mathcal{E}_{\mathcal{P} \rightarrow \mathcal{V}} \leftarrow \{(\mathcal{P}_{ij}, \mathcal{V}_i) \mid \mathbf{O}_{ij} = 1, i = 1, 2, \dots, m\}$
- 2: **if** \mathcal{V} provided **then**
- 3: $\hat{\mathcal{V}} \leftarrow \mathcal{V} + \text{GRAPHCROSSATTENTION}(\mathcal{P}, \mathcal{V}, \mathcal{E}_{\mathcal{P} \rightarrow \mathcal{V}}, d_p, d_v)$
- 4: **else**
- 5: $\hat{\mathcal{V}} \leftarrow \text{GRAPHCROSSATTENTION}(\mathcal{P}, \mathcal{E}_{\mathcal{P} \rightarrow \mathcal{V}}, d_p, d_v)$
- 6: $\hat{\mathcal{V}} \leftarrow \hat{\mathcal{V}} + \text{FFN}(\text{ReLU}(\text{LN}(\hat{\mathcal{V}})))$

Procedure 3 UPDATESCENEPOINTFEAT

Input: \mathcal{P}, \mathbf{O} Projection features + observability matrix.
Input: \mathcal{S} Previous scene point features (optional).
Input: d_p, d_s Feature dimensions.
Output: $\hat{\mathcal{S}}$ Updated scene point features.

- 1: $\mathcal{E}_{\mathcal{P} \rightarrow \mathcal{S}} \leftarrow \{(\mathcal{P}_{ij}, \mathcal{S}_i) \mid \mathbf{O}_{ij} = 1, i = 1, 2, \dots, m\}$
- 2: **if** \mathcal{S} provided **then**
- 3: $\hat{\mathcal{S}} \leftarrow \mathcal{S} + \text{GRAPHCROSSATTENTION}(\mathcal{P}, \mathcal{S}, \mathcal{E}_{\mathcal{P} \rightarrow \mathcal{S}}, d_p, d_s)$
- 4: **else**
- 5: $\hat{\mathcal{S}} \leftarrow \text{GRAPHCROSSATTENTION}(\mathcal{P}, \mathcal{E}_{\mathcal{P} \rightarrow \mathcal{S}}, d_p, d_s)$
- 6: $\hat{\mathcal{S}} \leftarrow \hat{\mathcal{S}} + \text{FFN}(\text{ReLU}(\text{LN}(\hat{\mathcal{S}})))$

out with two independent aggregations, with different learned parameters, and the sum of both aggregations constitute the residual mapping. Figure 4 provides an illustration for the update operation.

Projection Feature Update. The projection features are updated according to Procedure 5. No aggregation

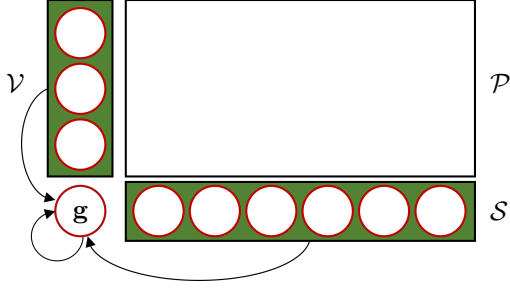


Figure 4. Illustration of the global feature update, where \mathbf{g} is updated based on its previous value, together with an aggregation of all \mathcal{V} and \mathcal{S} features.

Procedure 4 UPDATEGLOBALFEAT

Input: \mathcal{V} View features.

Input: \mathcal{S} Scene point features.

Input: \mathbf{g} Previous global features (optional).

Input: d_v, d_s, d_g Feature dimensions.

Output: $\hat{\mathbf{g}}$ Updated global features.

- 1: $\mathcal{E}_{\mathcal{V} \rightarrow \mathbf{g}} \leftarrow \{(\mathcal{V}_i, \mathbf{g}) \mid i = 1, 2, \dots, m\}$
 - 2: $\mathcal{E}_{\mathcal{S} \rightarrow \mathbf{g}} \leftarrow \{(\mathcal{S}_j, \mathbf{g}) \mid j = 1, 2, \dots, n\}$
 - 3: **if** \mathbf{g} provided **then**
 - 4: $\hat{\mathbf{g}}_v \leftarrow \text{GRAPHCROSSATTENTION}(\mathcal{V}, \{\mathbf{g}\}, \mathcal{E}_{\mathcal{V} \rightarrow \mathbf{g}}, d_v, d_g)$
 - 5: $\hat{\mathbf{g}}_s \leftarrow \text{GRAPHCROSSATTENTION}(\mathcal{S}, \{\mathbf{g}\}, \mathcal{E}_{\mathcal{S} \rightarrow \mathbf{g}}, d_s, d_g)$
 - 6: $\hat{\mathbf{g}} \leftarrow \mathbf{g} + \hat{\mathbf{g}}_v + \hat{\mathbf{g}}_s$
 - 7: **else**
 - 8: $\hat{\mathbf{g}}_v \leftarrow \text{GRAPHCROSSATTENTION}(\mathcal{V}, -, \mathcal{E}_{\mathcal{V} \rightarrow \mathbf{g}}, d_v, d_g)$
 - 9: $\hat{\mathbf{g}}_s \leftarrow \text{GRAPHCROSSATTENTION}(\mathcal{S}, -, \mathcal{E}_{\mathcal{S} \rightarrow \mathbf{g}}, d_s, d_g)$
 - 10: $\hat{\mathbf{g}} \leftarrow \hat{\mathbf{g}}_v + \hat{\mathbf{g}}_s$
 - 11: $\hat{\mathbf{g}} \leftarrow \hat{\mathbf{g}} + \text{FFN}(\text{ReLU}(\text{LN}(\hat{\mathbf{g}})))$
-

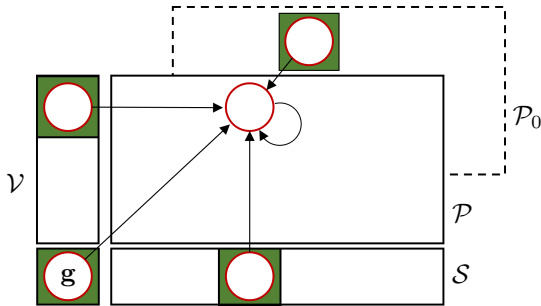


Figure 5. Illustration of the update of a single projection feature. All \mathcal{P} features are updated based on their previous value, as well as initial projection features \mathcal{P}_0 , the global feature \mathbf{g} , and the corresponding \mathcal{V} and \mathcal{S} features.

is involved during this step. Instead, at every projection node the corresponding \mathcal{V} , \mathcal{S} and \mathbf{g} features are all collected along with the current projection features \mathcal{P} , as illustrated in Figure 5. Each of these sources then undergoes a ReLU activation and normalization with LN, before being concatenated. Note that the initial projection features \mathcal{P}_0 are typically also added to the input, and in this case they are simply concatenated to the previous projection features before the procedure is called. Finally, a residual mapping is applied, by feeding the concatenated features to a shared feed-forward network.

Procedure 5 UPDATEPROJFEAT

Input: \mathcal{P} Previous projection features.

Input: \mathcal{V} View features.

Input: \mathcal{S} Scene point features.

Input: \mathbf{g} Global features.

Input: $d_p^{in}, d_v, d_s, d_g, d_p^{out}$ Feature dimensions.

Output: $\hat{\mathcal{P}}$ Updated projection features.

- 1: $\hat{\mathcal{P}} \leftarrow \text{ReLU}(\text{LN}(\mathcal{V})) \parallel \text{ReLU}(\text{LN}(\mathcal{S}))$
 $\parallel \text{ReLU}(\text{LN}(\mathbf{g})) \parallel \text{ReLU}(\text{LN}(\mathcal{P}))$ // View, scene point, and global features are implicitly distributed to their corresponding projection features before feature concatenation.
 - 2: $\hat{\mathcal{P}} \leftarrow \mathcal{P} + \text{FFN}_{(d_v+d_s+d_g+d_p^{in}) \rightarrow d_p^{out}}(\hat{\mathcal{P}})$
-

Entire Network Architecture.

Now we have all the pieces to define the complete network architecture, which is outlined in Procedure 6. The structure is straightforward: 1) UPDATEVIEWFEAT and UPDATESCENEPOINTFEAT (Procedures 2 and 3) are called to aggregate projection features. 2) UPDATEGLOBALFEAT (Procedure 4) is called to aggregate the resulting features further, to a single global feature vector. 3) UPDATEPROJFEAT (Procedure 5) is called in order to again distribute the aggregated information across the projection features. These steps are repeated L times, where we refer to L as the number of layers. Then, a final call to UPDATEVIEWFEAT and UPDATESCENEPOINTFEAT is carried out, and the resulting view and scene point features are further processed by two corresponding regression heads, consisting of shared 3-layer feed-forward networks (FFN) with hidden neurons of the same dimension as the input (d_v or d_s). The scene point head simply outputs the 3 coordinates of every estimated scene point. For Euclidean reconstruction, the view head outputs the 3 coordinates of the location of the camera center, together with a unit-norm quaternion representing its orientation. For projective reconstruction, all 12 camera matrix elements are regressed, followed by a normalization in the same manner as [31]. Except for the regression heads, we use 1-layer FFNs throughout the network, which in general seemed slightly easier to train.

3.2. Loss Function

The network is trained using the Adam optimizer, and as loss function we use the (non-squared) reprojection error, averaged over all observed image points. To handle negative depths and overcome the singularity at the principal plane, we substitute the reprojection error with minus the depth in the loss function for any projection with depth smaller than a threshold $h = 1e - 4$. We also apply gradient normalization in the same manner as [31].

3.3. Data Augmentation

For Euclidean reconstruction, where the image points are normalized using the intrinsic camera parameters, and therefore geometrically interpretable, we experi-

Procedure 6 GRAPHATTENTIONSFM

Input: \mathcal{M} Image point tracks, normalized.
Input: \mathbf{O} Observability matrix.
Input: d_p, d_v, d_s, d_g Feature dimensions.
Input: L Number of layers.
Output: \mathcal{V} Estimated camera parameters.
Output: \mathcal{S} Estimated scene points.

```
1:  $\mathcal{P}_0 \leftarrow \text{Linear}_{2 \rightarrow 2}(\mathcal{M})$  // Initial projection features:  
   linear embedding of image points.  
2:  $\mathcal{V} \leftarrow \text{UPDATEVIEWFEAT}(\mathcal{P}_0, \mathbf{O}, -, 2, d_v)$   
3:  $\mathcal{S} \leftarrow \text{UPDATESCENEPOINTFEAT}(\mathcal{P}_0, \mathbf{O}, -, 2, d_s)$   
4:  $\mathbf{g} \leftarrow \text{UPDATEGLOBALFEAT}(\mathcal{V}, \mathcal{S}, -, d_v, d_s, d_g)$   
5: for  $l = 1, 2, \dots, L$  do  
6:   if  $l = 1$  then  
7:      $\mathcal{P} \leftarrow \text{UPDATEPROJFEAT}(\mathcal{P}_0, \mathcal{V}, \mathbf{g}, 2, d_v, d_s, d_g, d_p)$   
8:   else  
9:      $\mathcal{P} \leftarrow \text{UPDATEPROJFEAT}(\mathcal{P} \parallel \mathcal{P}_0, \mathcal{V}, \mathbf{g},$   
10:     $d_p + 2, d_v, d_s, d_g, d_p)$   
11:    $\mathcal{V} \leftarrow \text{UPDATEVIEWFEAT}(\mathcal{P}, \mathbf{O}, \mathcal{V}, d_p, d_v)$   
12:    $\mathcal{S} \leftarrow \text{UPDATESCENEPOINTFEAT}(\mathcal{P}, \mathbf{O}, \mathcal{S}, d_p, d_s)$   
13:   if  $l < L$  then  
14:      $\mathbf{g} \leftarrow \text{UPDATEGLOBALFEAT}(\mathcal{V}, \mathcal{S}, \mathbf{g}, d_v, d_s, d_g)$   
15:  $\{\mathbf{P}_i\} \leftarrow \text{FFN}(\text{ReLU}(\mathcal{V}))$  // Camera regression head  
16:  $\{\mathbf{X}_j\} \leftarrow \text{FFN}(\text{ReLU}(\mathcal{S}))$  // Scene point regression  
   head
```

ment with augmenting the training scenes with slightly transformed variations. While the scene points remain fixed, each camera is randomly rotated about its center, first by a uniformly sampled angle $\alpha \in [-15, 15]$ about the principal axis, followed by a uniformly sampled angle $\gamma \in [-20, 20]$ about an axis orthogonal to the principal axis with a random direction. The image points are transformed accordingly.

3.4. Artificial Outlier Injection

We also consider the presence of measurement outliers, by artificially corrupting the data. This is done by: 1) Selecting a subset of the 2D keypoint measurements to be replaced by artificial outliers. 2) For each view, replace all measurements marked to be outliers with random samples from a bivariate normal distribution, which is fit to all remaining (inlier) points. For step 1), we carefully select points for outlier injection such that we avoid getting any scene points visible in < 2 views or any views with < 8 scene points visible, if regarding only the inlier projections. In the supplementary material, the details are given on how this is achieved. Note that while the network input is corrupted by outlier injection, the uncorrupted data is still used as learning targets for the loss function.

4. Results

4.1. Experimental Setup

We take a particular interest in Euclidean reconstruction, due to the relevance of metric reconstructions for photogrammetry applications. Furthermore, we focus mainly on the task of learning and generalizing from a set of training scenes, due to the great potential in having a fast learned model acquire reconstructions of

completely novel scenes. We use the DPESFM method of Moran et al. [31] as a baseline, as they have presented experiments on precisely this. To this end, we also use Olsson’s dataset [33] (together with the VGG dataset [12] for additional projective reconstruction experiments in the supplement), and we use the same random partition of 10 test scenes and 3 validation scenes.

We base our implementation on that of [31], implemented in PyTorch [34], but replace the network architecture with our proposed GRAPHATTENTIONSFM network, implemented using GATv2Conv layers [4] from PyTorch Geometric [11]. The implementation details are in general consistent with [31], for more details see the supplement. The DPESFM results reproduced by us are obtained by running the method of [31] with our code base, with the hyper-parameters published on the official GitHub repository of the method [30]. For our model, we use $L = 12$ layers and feature dimensions $d_p = 32, d_v = 1024, d_s = 64, d_g = 2048$, which corresponds to 145M parameters. By using small dimensions for the projection features and scene point features the otherwise high memory consumption is significantly reduced. Hyper-parameters have been chosen based on the performance on the validation data, but without any rigorous hyper-parameter tuning.

4.2. Euclidean Reconstruction of Novel Scenes

In Table 1, we report the Euclidean reconstruction results of our method, when applied on novel test scenes, and measure the performance by reprojection errors, as well as rotation and translation errors for the estimated camera poses. For calculating the latter, the predicted and ground truth poses are first aligned to a common reference frame, as described in Section C in the supplement. The results of DPESFM as reported in [31] can be seen in parentheses, when available, but we also re-train their model and incorporate further results of the model, not reported in [31], in particular results without bundle adjustment, and additional metrics to reprojection errors. Experiments are carried out both with and without data augmentation with random rotational cameras perturbations, as described in Section 3.3, and the columns are partitioned accordingly. Consistently with [31], *Inference* refers to the network output followed by a computationally cheap triangulation and *Inference + BA* refers to the network output followed by bundle adjustment, which is carried out in the same manner as [31], using the Ceres solver [1]. Moran et al. [31] also performed experiments with fine-tuning the network parameters on the test scenes. In contrast, we advocate against this, since this approach is relatively costly, and one might as well acquire high-quality reconstructions from traditional SfM pipelines such as Colmap, in similar execution time. Nevertheless, the supplementary material includes such experiments, for completeness.

Without data augmentation, there is no clear differ-

	Without data augmentation				With data augmentation				Colmap	
	Inference		Inference + BA		Inference		Inference + BA			
	Ours	DPESFM	Ours	DPESFM	Ours	DPESFM	Ours	DPESFM		
Reprojection error (px)	Alcatraz Courtyard	68.41	68.50	1.70	0.81 (0.82)	36.01	92.37	0.81	0.92	0.81
	Alcatraz Water Tower	36.30	50.47	1.05	1.13 (0.55)	87.67	2831.94	0.88	10.16	0.55
	Drinking Fountain Somewhere in Zurich	36.02	45.87	0.55	0.31 (7.21)	219.75	234.90	0.31	6.73	0.31
	Nijo Castle Gate	65.71	64.53	0.73	0.73 (5.81)	61.41	68.19	0.88	0.89	0.73
	Porta San Donato Bologna	74.32	94.26	0.74	0.74 (1.10)	52.15	84.46	0.76	0.75	0.75
	Round Church Cambridge	61.18	55.51	0.39	0.39 (0.50)	29.80	59.54	0.39	1.49	0.39
	Smolny Cathedral St Petersburg	156.16	120.85	0.81	0.81 (15.15)	85.38	87.81	0.81	0.81	0.81
	Some Cathedral in Barcelona	150.01	146.10	10.42	12.71 (21.46)	125.68	687.83	0.89	16.77	0.89
	Sri Veeramakaliamman Singapore	121.02	157.39	2.19	16.87 (16.92)	83.50	166.68	2.13	9.30	0.71
	Yueh Hai Ching Temple Singapore	37.46	52.59	0.65	0.65 (1.16)	25.60	51.35	0.65	0.73	0.65
	Average	80.66	85.61	1.92	3.52 (7.07)	80.69	436.51	0.85	4.86	0.66
Rotation error (deg)	Alcatraz Courtyard	10.102	13.201	2.607	0.035	6.093	10.946	0.038	0.030	0.043
	Alcatraz Water Tower	10.637	11.053	0.499	0.764	11.501	10.641	0.699	19.351	0.228
	Drinking Fountain Somewhere in Zurich	15.846	16.014	0.003	0.001	15.415	15.704	0.001	22.759	0.007
	Nijo Castle Gate	16.751	10.546	0.062	0.062	17.347	20.032	0.038	0.036	0.064
	Porta San Donato Bologna	23.839	24.120	0.095	0.094	18.411	25.004	0.094	0.094	0.099
	Round Church Cambridge	18.906	14.473	0.029	0.026	10.295	18.685	0.029	1.086	0.035
	Smolny Cathedral St Petersburg	19.387	17.971	0.023	0.022	11.662	14.380	0.023	0.019	0.029
	Some Cathedral in Barcelona	27.270	30.471	10.009	20.050	27.908	29.119	0.020	47.892	0.025
	Sri Veeramakaliamman Singapore	28.275	36.903	0.549	4.871	23.702	36.176	0.457	2.759	0.169
	Yueh Hai Ching Temple Singapore	15.733	22.706	0.038	0.038	9.515	21.561	0.038	0.038	0.043
	Average	18.675	19.746	1.391	2.596	15.185	20.225	0.144	9.406	0.074
Translation error (m)	Alcatraz Courtyard	4.82	4.93	1.09	0.01	2.73	5.74	0.01	0.01	0.01
	Alcatraz Water Tower	8.66	7.35	0.31	0.44	7.53	7.77	0.41	9.05	0.12
	Drinking Fountain Somewhere in Zurich	4.44	4.44	0.00	0.00	4.45	4.46	0.00	1.38	0.00
	Nijo Castle Gate	5.07	3.08	0.01	0.01	5.67	6.95	0.01	0.01	0.01
	Porta San Donato Bologna	9.50	10.72	0.05	0.05	4.80	10.48	0.05	0.05	0.05
	Round Church Cambridge	8.94	7.19	0.01	0.01	5.28	9.00	0.01	0.56	0.01
	Smolny Cathedral St Petersburg	2.70	2.43	0.01	0.01	2.33	2.52	0.01	0.01	0.01
	Some Cathedral in Barcelona	12.64	12.69	3.22	6.38	12.32	12.66	0.01	11.93	0.01
	Sri Veeramakaliamman Singapore	4.94	4.90	0.16	1.32	4.93	4.90	0.14	0.77	0.04
	Yueh Hai Ching Temple Singapore	4.12	4.27	0.01	0.01	2.44	4.28	0.01	0.01	0.01
	Average	6.58	6.20	0.49	0.82	5.25	6.88	0.07	2.38	0.03

Table 1. Results of Euclidean reconstruction of novel test scenes, with and without data augmentation. The results of DPESFM [31] have been acquired by us training the model, along with the results reported by [31] in parentheses, if available. The result of Colmap, as reported by [31], is also added for reference.

Scene	Infer.	BA	Colmap
Alcatraz Courtyard	0.24	45.54	286
Alcatraz Water Tower	0.13	31.11	130
Drinking Fountain Somewhere In Zurich	0.06	1.98	16
Nijo Castle Gate	0.09	3.97	21
Porta San Donato Bologna	0.18	27.02	170
Round Church Cambridge	0.43	56.47	229
Smolny Cathedral St Petersburg	0.49	86.09	516
Some Cathedral In Barcelona	0.24	47.05	451
Sri Veeramakaliamman Singapore	0.63	115.80	583
Yueh Hai Ching Temple Singapore	0.08	8.54	106

Table 2. Runtime (s) of our method for Euclidean reconstruction on test scenes, in comparison with Colmap (measured by [31]).

ence between the *Inference* results of both methods. Neither reconstruction is good, and it is not so meaningful to compare minor differences in the metrics under these circumstances. In particular, calculating rotation and translation errors requires aligning the predicted and ground truth camera poses in a common reference frame, as described in Section C in the supplement, and when the predicted configuration of camera poses is not very consistent with the ground truth, determining this alignment itself can be sensitive. In all other scenarios, we outperform DPESFM, and when using both data augmentation and applying bundle adjustment, the solu-

tions we acquire for the novel test scenes are in general very good. In terms of reprojection error and translation error, we match the performance of Colmap for almost every test scene, leading to an average reprojection error of 0.85 (vs 0.66) px, and an average translation error of 0.07 (vs 0.03) m. In terms of rotation error, the error is actually lower than Colmap’s for 8 out of 10 scenes, but the average error is slightly larger: 0.144 (vs 0.074) degrees.

4.3. Artificial Outlier Injection

In Table 3 we present additional results where, on top of data augmentation (see Section 3.3), we also apply artificial outlier injection during training according to Section 3.4.

We evaluate inference of the model in two settings: 1) Applied on the uncorrupted outlier-free test scenes as-is. 2) Applied to the test scenes followed by random injection of 10%, in the same manner as during training². One can immediately observe significantly reduced reprojection errors for our model, suggesting that the outlier injection during training has a regularizing effect. Beyond that, this experiment is intended to

²Yet, during evaluation, we use all true measurements as ground truth targets when calculating reprojection errors, even in the corrupted case.

	Uncorrupted		Outlier-injected	
	Ours	DPESFM	Ours	DPESFM
Alcatraz Courtyard	47.74	85.81	52.99	94.24
Alcatraz Water Tower	35.96	72.84	37.89	83.55
Drinking Fountain Somewhere in Zurich	52.08	1012.14	46.65	1453.31
Nijo Castle Gate	46.48	72.99	62.52	126.18
Porta San Donato Bologna	53.12	88.02	65.08	94.72
Round Church Cambridge	36.09	63.72	48.63	90.63
Smolny Cathedral St Petersburg	47.28	91.03	59.52	98.05
Some Cathedral in Barcelona	109.86	397.75	123.75	462.28
Sri Veeramakali- amman Singapore	63.60	169.63	70.90	146.98
Yueh Hai Ching Temple Singapore	26.83	51.41	36.69	57.59
Average	51.91	210.53	60.46	270.75

Table 3. Reprojection errors of Euclidean reconstruction of novel test scenes, with model trained with data augmentation as well as artificial outlier injection. The results of DPESFM [31] have been acquired by us training the model.

serve as a teaser for the utility and promise of learning-based methods for SfM. Constant challenges such as the presence of outliers may not be as big of a challenge for learning-based as for conventional methods, and the phenomenon may even be exploited to develop effective training strategies. In fact, for any real-world scenario, it is crucial for learning-based methods applied on image point correspondences to be resilient to outliers, as we do not have the luxury of facing high-quality curated data such as Olsson’s [33] in the wild. Note that it should be possible to apply bundle adjustment on the corrupted test data as well, when combined with a robust loss function.

Similarly as for the data augmentation, we note that DPESFM appears to struggle with the presence of outliers during training, and its performance on the test scenes at inference is not very good. It is very probable that the nonlinear attention layers make our model more powerful and expressive than DPESFM.

4.4. Additional Results

In the supplementary material we provide additional results on projective reconstruction, as well as single-scene optimization, for completeness. We also include statistics of the number of views and scene points for each scene.

5. Conclusion

With this paper we have added to the research direction of learned initialization-free Structure-from-Motion by introducing a novel and expressive graph attention network outperforming previous learning-based methods for Euclidean reconstruction of novel scenes. When succeeded by bundle adjustment, we are able to recon-

struct novel test scenes to perfection or of very decent precision, at a speedup of about 5 – 10× compared to Colmap. Moreover, we illustrate great potential in coping with the presence of outliers, and even show artificial outlier injection to provide an effective regularizing training strategy, combined with data augmentation by random rotational camera perturbations.

For future work, it could definitely be promising to train on larger datasets, since model generalization is still a challenge. While the proposed model does not require fine-tuning, and thus is much faster to execute than previous work, it still relies on bundle adjustment to acquire a good reconstruction, which constitutes the computational bottleneck. Exploring alternative formulations where the network regresses relative camera poses is also an interesting direction, as the current absolute pose prediction may be a weakness due to the reconstruction ambiguity up to a similarity transformation. Other possible research directions include unrolling the architecture to multiple learned iterations / refinement steps, extensions to non-rigid Structure-from-Motion, and incorporating modern learned image matching pipelines such as [5, 6, 40] in an end-to-end fashion.

Acknowledgements The work was supported by the Wallenberg AI, Autonomous Systems and Software Program (WASP) funded by the Knut and Alice Wallenberg Foundation, and the Swedish Research Council grants no. 2016-04445, 2018-05375, and 2023-05341. Computations were enabled by resources provided by the National Academic Infrastructure for Supercomputing in Sweden (NAISS) at Chalmers Centre for Computational Science and Engineering (C3SE) and National Supercomputer Centre (NSC) Berzelius at Linköping University partially funded by the Swedish Research Council through grant no. 2022-06725.

References

- [1] Sameer Agarwal, Keir Mierle, and Others. Ceres solver. <http://ceres-solver.org/>. 6
- [2] Sameer Agarwal, Noah Snavely, Ian Simon, Steven M. Seitz, and Richard Szeliski. Building rome in a day. In *2009 IEEE 12th International Conference on Computer Vision*, pages 72–79, 2009. 1
- [3] Jimmy Lei Ba, Jamie Ryan Kiros, and Geoffrey E. Hinton. Layer normalization, 2016. 3
- [4] Shaked Brody, Uri Alon, and Eran Yahav. How attentive are graph attention networks? In *International Conference on Learning Representations*, 2022. 2, 4, 6
- [5] Georg Bökman and Fredrik Kahl. A case for using rotation invariant features in state of the art feature matchers. In *Proceedings of the IEEE/CVF Conference on Computer Vision and Pattern Recognition*, pages 5110–5119, 2022. 8
- [6] Georg Bökman, Johan Edstedt, Michael Felsberg, and Fredrik Kahl. Steerers: A framework for rotation equivariant keypoint descriptors. In *IEEE Conf. Comput. Vis. Pattern Recog.*, 2024. 8
- [7] Anpei Chen, Zexiang Xu, Andreas Geiger, Jingyi Yu, and Hao Su. *TensorRF: Tensorial Radiance Fields*, pages 333–350. 2022. 2
- [8] Yuchao Dai, Hongdong Li, and Mingyi He. Projective multiview structure and motion from element-wise factorization. *IEEE Transactions on Pattern Analysis and Machine Intelligence*, 35(9):2238–2251, 2013. 1
- [9] Olof Enqvist, Fredrik Kahl, and Carl Olsson. Non-sequential structure from motion. In *2011 IEEE International Conference on Computer Vision Workshops (ICCV Workshops)*, pages 264–271, 2011. 1
- [10] Anders Eriksson, Carl Olsson, Fredrik Kahl, and Tat-Jun Chin. Rotation averaging with the chordal distance: Global minimizers and strong duality. *IEEE Trans. Pattern Anal. Mach. Intell.*, 43(1):256–268, 2021. 1
- [11] Matthias Fey and Jan E. Lenssen. Fast graph representation learning with PyTorch Geometric. In *ICLR Workshop on Representation Learning on Graphs and Manifolds*, 2019. 4, 6
- [12] Oxford Visual Geometry Group. Multi-view datasets. <https://www.robots.ox.ac.uk/~vgg/data/mview/>. 6
- [13] Richard Hartley. In defense of the eight-point algorithm. *IEEE Transactions on Pattern Analysis and Machine Intelligence*, 19(6):580–593, 1997. 1, 2
- [14] Richard Hartley and Fredrik Kahl. Critical configurations for projective reconstruction from multiple views. *Int. J. Comput. Vis.*, 71(1):5–47, 2007.
- [15] Richard Hartley and Andrew Zisserman. *Multiple View Geometry in Computer Vision*. Cambridge University Press, 2 edition, 2004. 1
- [16] Je Hyeong Hong, Christopher Zach, Andrew Fitzgibbon, and Roberto Cipolla. Projective bundle adjustment from arbitrary initialization using the variable projection method. In *ECCV 2016*, pages 477–493. Springer, 2016. 2, 9
- [17] Je Hyeong Hong, Christopher Zach, and Andrew Fitzgibbon. Revisiting the variable projection method for separable nonlinear least squares problems. In *2017 IEEE Conference on Computer Vision and Pattern Recognition (CVPR)*, pages 5939–5947, 2017. 1
- [18] José Pedro Iglesias, Amanda Nilsson, and Carl Olsson. expOSE: Accurate initialization-free projective factorization using exponential regularization. In *IEEE Conf. Comput. Vis. Pattern Recog.*, pages 8959–8968, 2023. 1
- [19] Nianjuan Jiang, Zhaopeng Cui, and Ping Tan. A global linear method for camera pose registration. In *Proceedings of the IEEE International Conference on Computer Vision (ICCV)*, 2013. 3, 6, 7, 8
- [20] Fredrik Kahl and Richard Hartley. Multiple view geometry under the L_∞ -norm. *IEEE Trans. Pattern Anal. Mach. Intell.*, 30(9):1603–1617, 2008. 1
- [21] Fredrik Kahl, Richard Hartley, and Kalle Astrom. Critical configurations for n-view projective reconstruction. In *IEEE Conf. Comput. Vis. Pattern Recog.*, 2001.
- [22] Fredrik Kahl, Sameer Agarwal, Manmohan Chandraker, David Kriegman, and Serge Belongie. Practical global optimization for multiview geometry. *Int. J. Comput. Vis.*, 79(3):271–284, 2008. 1
- [23] Yoni Kasten, Amnon Geifman, Meirav Galun, and Ronen Basri. Gpsfm: Global projective sfm using algebraic constraints on multi-view fundamental matrices. In *Proceedings of the IEEE/CVF Conference on Computer Vision and Pattern Recognition (CVPR)*, 2019. 9
- [24] Yoni Kasten, Amnon Geifman, Meirav Galun, and Ronen Basri. Algebraic characterization of essential matrices and their averaging in multiview settings. In *Proceedings of the IEEE/CVF International Conference on Computer Vision (ICCV)*, 2019. 3, 6, 7, 8
- [25] Q. Ke and T. Kanade. Quasiconvex optimization for robust geometric reconstruction. *IEEE Trans. Pattern Anal. Mach. Intell.*, 29(10):1834–1847, 2007. 1
- [26] Diederik P. Kingma and Jimmy Ba. Adam: A method for stochastic optimization. In *3rd International Conference on Learning Representations, ICLR 2015, San Diego, CA, USA, May 7-9, 2015, Conference Track Proceedings*, 2015. 2
- [27] Kurt Konolige. Sparse sparse bundle adjustment. In *Brit. Mach. Vis. Conf.*, pages 1–11, 2010. 1
- [28] Ludovic Magerand and Alessio Del Bue. Practical projective structure from motion (p2sfm). In *Int. Conf. Comput. Vis.*, pages 39–47, 2017. 1, 9
- [29] Ben Mildenhall, Pratul P. Srinivasan, Matthew Tancik, Jonathan T. Barron, Ravi Ramamoorthi, and Ren Ng. Nerf: Representing scenes as neural radiance fields for view synthesis, 2020. cite arxiv:2003.08934Comment: ECCV 2020 (oral). Project page with videos and code: <http://tancik.com/nerf>. 2
- [30] Dror Moran, Hodaya Koslowsky, Yoni Kasten, Haggai Maron, Meirav Galun, and Ronen Basri. Deep permutation-equivariant sfm: Github repository. <https://github.com/drormoran/Equivariant-SFM/>. 6
- [31] Dror Moran, Hodaya Koslowsky, Yoni Kasten, Haggai Maron, Meirav Galun, and Ronen Basri. Deep permutation equivariant structure from motion. In *Proceedings of the IEEE/CVF International Conference on Computer Vision (ICCV)*, pages 5976–5986, 2021. 2, 5, 6, 7, 8, 1, 3, 4, 9, 10, 11, 12, 13, 14, 15, 16, 17, 18, 19

- [32] David Nister. An efficient solution to the five-point relative pose problem. *IEEE Transactions on Pattern Analysis and Machine Intelligence*, 26(6):756–770, 2004. 1
- [33] Carl Olsson and Olof Enqvist. Stable structure from motion for unordered image collections. In *Scand. Conf. Image Analysis*, pages 524–535. Springer, 2011. 6, 8
- [34] Adam Paszke, Sam Gross, Francisco Massa, Adam Lerer, James Bradbury, Gregory Chanan, Trevor Killeen, Zeming Lin, Natalia Gimelshein, Luca Antiga, Alban Desmaison, Andreas Kopf, Edward Yang, Zachary DeVito, Martin Raison, Alykhan Tejani, Sasank Chilamkurthy, Benoit Steiner, Lu Fang, Junjie Bai, and Soumith Chintala. Pytorch: An imperative style, high-performance deep learning library. In *Advances in Neural Information Processing Systems 32*, pages 8024–8035. Curran Associates, Inc., 2019. 6
- [35] Pulak Purkait, Tat-Jun Chin, and Ian Reid. Neurora: Neural robust rotation averaging. In *Computer Vision – ECCV 2020*, pages 137–154, Cham, 2020. Springer International Publishing. 2
- [36] Johannes L. Schönberger. Colmap code. <https://colmap.github.io/>. 3, 6, 7, 8
- [37] Johannes Lutz Schönberger and Jan-Michael Frahm. Structure-from-motion revisited. In *Conference on Computer Vision and Pattern Recognition (CVPR)*, 2016. 1
- [38] Johannes Lutz Schönberger, Enliang Zheng, Marc Pollefeys, and Jan-Michael Frahm. Pixelwise view selection for unstructured multi-view stereo. In *European Conference on Computer Vision (ECCV)*, 2016. 1, 3, 6, 7, 8
- [39] Peter Sturm and Bill Triggs. A factorization based algorithm for multi-image projective structure and motion. In *Computer Vision — ECCV '96*, pages 709–720, Berlin, Heidelberg, 1996. Springer Berlin Heidelberg. 1
- [40] Jiaming Sun, Zehong Shen, Yuang Wang, Hujun Bao, and Xiaowei Zhou. LoFTR: Detector-free local feature matching with transformers. In *IEEE Conf. Comput. Vis. Pattern Recog.*, pages 8922–8931, 2021. 8
- [41] Bill Triggs, Philip F. McLauchlan, Richard I. Hartley, and Andrew W. Fitzgibbon. Bundle adjustment - a modern synthesis. page 298–372, Berlin, Heidelberg, 1999. Springer-Verlag. 1
- [42] Ashish Vaswani, Noam Shazeer, Niki Parmar, Jakob Uszkoreit, Llion Jones, Aidan N Gomez, Łukasz Kaiser, and Illia Polosukhin. Attention is all you need. In *Advances in Neural Information Processing Systems*. Curran Associates, Inc., 2017. 4
- [43] Petar Veličković, Guillem Cucurull, Arantxa Casanova, Adriana Romero, Pietro Liò, and Yoshua Bengio. Graph attention networks. In *International Conference on Learning Representations*, 2018. 2
- [44] Jianyuan Wang, Christian Rupprecht, and David Novotny. PoseDiffusion: Solving pose estimation via diffusion-aided bundle adjustment. 2023. 2
- [45] Zirui Wang, Shangzhe Wu, Weidi Xie, Min Chen, and Victor Adrian Prisacariu. NeRF—: Neural radiance fields without known camera parameters. *arXiv preprint arXiv:2102.07064*, 2021.
- [46] Xingkui Wei, Yinda Zhang, Zhuwen Li, Yanwei Fu, and Xiangyang Xue. DeepSfm: Structure from motion via deep bundle adjustment. In *ECCV*, 2020. 2
- [47] Yi Wei, Shaohui Liu, Yongming Rao, Wang Zhao, Jiwen Lu, and Jie Zhou. Nerfingmvs: Guided optimization of neural radiance fields for indoor multi-view stereo. In *ICCV*, 2021. 2
- [48] Christopher Zach and Je Hyeong Hong. pOSE: Pseudo object space error for initialization-free bundle adjustment. In *2018 IEEE/CVF Conference on Computer Vision and Pattern Recognition*, pages 1876–1885, 2018. 1

Learning Structure-from-Motion with Graph Attention Networks

Supplementary Material

In this supplementary material, we provide additional implementation details (Section A), dataset statistics (Section B), and some elaboration on alignment between estimated and ground truth camera poses carried out in certain cases (Section C). Finally, additional results are presented in Section D, including visualizations of the reconstructions quantitatively evaluated in the main paper.

A. Implementation Details

A.1. Artificial Outlier Injection Details

Here we explain the scheme we use when choosing which keypoints to corrupt with artificial outliers:

1. Define a desired outlier rate η , which we set to 10% in our experiments.
2. Mark all keypoints in views with ≤ 8 scene points visible as inliers, and do the same for all projections of scene points visible in ≤ 2 views. Let N denote the total number of keypoints, and $n_{fixed.inliers}$ denote the number of keypoints marked as inliers here.
3. From the $N - n_{fixed.inliers}$ remaining keypoints, take a random sample of candidates for outlier injection. In order not to violate the view and scene point lower bounds, some of these may not be accepted as candidates, so we add some margin on the number of keypoints selected. If selecting $n_{sel.target}$ out of the remaining $N - n_{fixed.inliers}$ candidates, i.e. a fraction of $\nu = \frac{n_{sel.target}}{N - n_{fixed.inliers}}$, would result in the desired outlier rate η , we instead sample a fraction according to the harmonic average of ν and 1, i.e. $1/(0.5 \cdot \frac{1}{\nu} + 0.5 \cdot \frac{1}{1})$.
4. We now determine whether the lower bounds would be violated for any views or scene points, by marking the candidates as outliers. If so, all projections corresponding to any of those views or scene points are instead fixed to be inliers.
5. If the remaining number of outlier candidates are still enough to meet the desired outlier rate, a random sample of the candidates is selected, to achieve exactly the desired rate η . If the number of candidates are not enough, we repeat steps 3.-4. until the condition is met.

A.2. Training and Learning Rate Schedule

We train our model for 40k epochs and perform validation every 250 epochs. Since we are using an attention-based model, we warm up the learning rate for 2500 iterations, linearly from 0 to $1e-4$. Then we apply an exponential learning rate decay corresponding to a factor of 10 every 250k iterations. In case of fine-tuning, the learning rate is kept constant at $1e-4$ through all 1000

iterations. By the same approach as [31], we randomly sample partial scenes during training, with subsequences of 10-20 views.

A.3. Computational Resources

We carry out our experiments on a compute cluster with Nvidia A40 GPUs.

A.4. Post-Processing

Post-processing of the network output is done in the same manner as [31]. That is, either a cheap DLT triangulation is carried out, often improving the quality of the reconstruction, or bundle adjustment (BA) is carried out. BA, if applied, is carried out with Huber loss with threshold 0.1, and in two rounds interleaved with triangulation, according to [31]. This also tends to improve the final results a bit, if global convergence is not achieved during the first round. Each round of BA is limited to 100 iterations.

B. Dataset Statistics

In Tables 4 and 5 we report the number of views and scene points for each of the Euclidean and projective scenes, respectively.

C. Camera Pose Alignment

For both Euclidean and projective reconstruction, there is always a respective inherent ambiguity regarding the choice of coordinate frame. The loss function that we use is invariant to the choice of coordinate frame, but we also carry out quantitative and qualitative evaluations of the reconstructed scene points and estimated camera poses in the Euclidean setting. In order to do so, however, one first needs to determine what coordinate frame to use. To this end, in the same manner as [31], we fit a similarity transformation between estimated and ground truth camera poses, by which the two may be aligned. It is, however, worth noting that this is not done with a lot of care / robustness, and the alignment may be quite arbitrary in case the pose estimates are inaccurate.

D. Additional Results

D.1. Euclidean Reconstruction of Novel Scenes

In addition to the Euclidean reconstruction results presented in Section 4.2, which focused on network inference followed by bundle adjustment, in this section we also consider fine-tuning of the network parameters on the novel scenes, before carrying out bundle adjustment. Fine-tuning is initialized with the model parameters at the epoch of minimal average reprojection error on the

	#Views	#Scene Points
Alcatraz Courtyard	133	23674
Alcatraz Water Tower	172	14828
Buddah Tooth Relic Temple Singapore	162	27920
Doge Palace Venice	241	67107
Door Lund	12	17650
Drinking Fountain Somewhere in Zurich	14	5302
East Indiaman Goteborg	179	25655
Ecole Superior De Guerre	35	13477
Eglise Du Dome	85	84792
Folke Filbyter	40	21150
Fort Channing Gate Singapore	27	23627
Golden Statue Somewhere in Hong Kong	18	39989
Gustav II Adolf	57	5813
Gustav Vasa	18	4249
Jonas Ahlstromer	40	2021
King 's College University of Toronto	77	7087
Lund University Sphinx	70	32668
Nijo Castle Gate	19	7348
Pantheon Paris	179	29383
Park Gate Clermont Ferrand	34	9099
Plaza De Armas Santiago	240	26969
Porta San Donato Bologna	141	25490
Round Church Cambridge	92	84643
Skansen Kronan Gothenburg	131	28371
Smolny Cathedral St Petersburg	131	51115
Some Cathedral in Barcelona	177	30367
Sri Mariamman Singapore	222	56220
Sri Thendayuthapani Singapore	98	88849
Sri Veeramakaliamman Singapore	157	130013
Statue Of Liberty	134	49250
The Pumpkin	196	69341
Thian Hook Keng Temple Singapore	138	34288
Tsar Nikolai I	98	37857
Urban II	96	22284
Vercingetorix	69	10754
Yueh Hai Ching Temple Singapore	43	13774

Table 4. Number of views and scene points for the Euclidean scenes.

validation set. It should be stressed that this optimization is very costly, and not something that we advocate. We merely present these experiments to provide a complete comparison with DPESFM [31]. Table 6 presents reprojection errors, rotation errors and translation errors for models trained without data augmentation, and Table 7 presents corresponding results with data augmentation. The *Inference* and *Inference BA* results are the same as presented in Section 4.2, but now presented side-by-side with the results of 1000 iterations of fine-tuning (the *Fine-tune* column), followed by bundle adjustment (column *Fine-tune + BA*). During fine-tuning, the same loss function is used as during training, but now minimized on the test scene. For both our method and DPESFM [31], fine-tuning can be used to improve the precision of the reconstruction further, and the results of our model trained with data augmentation and succeeded by bundle adjustment are then on par with Colmap.

	#Views	#Scene Points
Alcatraz Courtyard	133	23674
Alcatraz Water Tower	172	14828
Alcatraz West Side Gardens	419	65072
Basilica Di San Petronio	334	46035
Buddah Statue	322	156356
Buddah Tooth Relic Temple Singapore	162	27920
Corridor	11	737
Dinosaur 319	36	319
Dinosaur 4983	36	4983
Doge Palace Venice	241	67107
Drinking Fountain Somewhere in Zurich	14	5302
East Indiaman Goteborg	179	25655
Ecole Superior De Guerre	35	13477
Eglise Du Dome	85	84792
Folke Filbyter	40	21150
Golden Statue Somewhere in Hong Kong	18	39989
Gustav II Adolf	57	5813
Gustav Vasa	18	4249
Jonas Ahlstromer	40	2021
King 's College University of Toronto	77	7087
Lund University Sphinx	70	32668
Model House	10	672
Nijo Castle Gate	19	7348
Pantheon Paris	179	29383
Park Gate Clermont Ferrand	34	9099
Plaza De Armas Santiago	240	26969
Porta San Donato Bologna	141	25490
Skansen Kronan Gothenburg	131	28371
Skansen Lejonet Gothenburg	368	74423
Smolny Cathedral St Petersburg	131	51115
Some Cathedral in Barcelona	177	30367
Sri Mariamman Singapore	222	56220
Sri Thendayuthapani Singapore	98	88849
Sri Veeramakaliamman Singapore	157	130013
The Pumpkin	195	69335
Thian Hook Keng Temple Singapore	138	34288
Tsar Nikolai I	98	37857
Urban II	96	22284

Table 5. Number of views and scene points for the projective scenes.

D.2. Projective Reconstruction of Novel Scenes

In addition to the Euclidean reconstruction results presented in Section 4.2, in Table 8 we also present corresponding results for projective reconstruction, along with a comparison to DPESFM [31] and VarPro [16]. In Table 9, the respective execution times are reported. In the projective setting we also feed normalized image point correspondences as input to the model but, like [31], use Hartley normalization [13] instead of the intrinsic camera parameters. Note that no data augmentation is applied in the projective setting. While doing so with random homography transformations would be feasible, determining a distribution over transformations would not be geometrically interpretable in the same way as for the Euclidean setting, and thus less straightforward. It can be noted that both our method and DPESFM perform worse at inference of test scenes in the projective setting, as compared to the Euclidean one, but for both methods bundle adjustment still converges to relatively good solutions.

	Inference		Inference + BA		Fine-tune		Fine-tune + BA		Colmap	
	Ours	DPESFM	Ours	DPESFM	Ours	DPESFM	Ours	DPESFM		
Reprojection error (px)	Alcatraz Courtyard	68.41	68.50	1.70	0.81 (0.82)	2.90	5.92	0.81	0.81 (0.81)	0.81
	Alcatraz Water Tower	36.30	50.47	1.05	1.13 (0.55)	5.83	147.83	0.55	8.63 (0.55)	0.55
	Drinking Fountain Somewhere in Zurich	36.02	45.87	0.55	0.31 (7.21)	0.62	27.43	0.31	6.73 (0.31)	0.31
	Nijo Castle Gate	65.71	64.53	0.73	0.73 (5.81)	3.82	5.22	0.73	0.73 (0.73)	0.73
	Porta San Donato Bologna	74.32	94.26	0.74	0.74 (1.10)	4.42	9.37	0.74	0.74 (0.79)	0.75
	Round Church Cambridge	61.18	55.51	0.39	0.39 (0.50)	3.92	5.92	0.39	1.50 (1.51)	0.39
	Smolny Cathedral St Petersburg	156.16	120.85	0.81	0.81 (15.15)	3.33	6.68	0.81	0.81 (0.81)	0.81
	Some Cathedral in Barcelona	150.01	146.10	10.42	12.71 (21.46)	7.99	27.80	0.89	0.89 (0.89)	0.89
	Sri Veeramakaliamman Singapore	121.02	157.39	2.19	16.87 (16.92)	25.06	40.76	1.20	0.88 (17.26)	0.71
	Yueh Hai Ching Temple Singapore	37.46	52.59	0.65	0.65 (1.16)	2.84	8.27	0.65	0.65 (0.65)	0.65
	Average	80.66	85.61	1.92	3.52 (7.07)	6.07	28.52	0.71	2.24 (2.43)	0.66
Rotation error (deg)	Alcatraz Courtyard	10.102	13.201	2.607	0.035	1.822	1.423	0.038	0.038	0.043
	Alcatraz Water Tower	10.637	11.053	0.499	0.764	4.161	18.217	0.228	22.764	0.228
	Drinking Fountain Somewhere in Zurich	15.846	16.014	0.003	0.001	0.453	19.678	0.001	22.776	0.007
	Nijo Castle Gate	16.751	10.546	0.062	0.062	2.301	3.326	0.064	0.064	0.064
	Porta San Donato Bologna	23.839	24.120	0.095	0.094	3.664	3.410	0.094	0.094	0.099
	Round Church Cambridge	18.906	14.473	0.029	0.026	6.720	3.116	0.028	1.089	0.035
	Smolny Cathedral St Petersburg	19.387	17.971	0.023	0.022	2.969	2.311	0.023	0.023	0.029
	Some Cathedral in Barcelona	27.270	30.471	10.009	20.050	3.874	18.440	0.019	0.019	0.025
	Sri Veeramakaliamman Singapore	28.275	36.903	0.549	4.871	15.083	30.726	0.218	0.184	0.169
	Yueh Hai Ching Temple Singapore	15.733	22.706	0.038	0.038	3.392	4.624	0.038	0.038	0.043
	Average	18.675	19.746	1.391	2.596	4.444	10.527	0.075	4.709	0.074
Translation error (m)	Alcatraz Courtyard	4.82	4.93	1.09	0.01	0.49	0.48	0.01	0.01	0.01
	Alcatraz Water Tower	8.66	7.35	0.31	0.44	2.19	8.61	0.12	9.60	0.12
	Drinking Fountain Somewhere in Zurich	4.44	4.44	0.00	0.00	0.04	2.58	0.00	1.38	0.00
	Nijo Castle Gate	5.07	3.08	0.01	0.01	0.49	0.79	0.01	0.01	0.01
	Porta San Donato Bologna	9.50	10.72	0.05	0.05	0.70	0.83	0.05	0.05	0.05
	Round Church Cambridge	8.94	7.19	0.01	0.01	1.86	1.41	0.01	0.56	0.01
	Smolny Cathedral St Petersburg	2.70	2.43	0.01	0.01	0.14	0.24	0.01	0.01	0.01
	Some Cathedral in Barcelona	12.64	12.69	3.22	6.38	1.30	7.72	0.01	0.01	0.01
	Sri Veeramakaliamman Singapore	4.94	4.90	0.16	1.32	3.07	4.65	0.05	0.05	0.04
	Yueh Hai Ching Temple Singapore	4.12	4.27	0.01	0.01	0.41	1.04	0.01	0.01	0.01
	Average	6.58	6.20	0.49	0.82	1.07	2.84	0.03	1.17	0.03

Table 6. Euclidean reconstruction of novel test scenes, with model trained without data augmentation. The results of DPESFM [31] have been acquired by us training the model, along with the results reported by [31] in parentheses, if available. The result of Colmap, as reported by [31], is also added for reference.

D.3. Single-Scene Recovery

While not of major interest to us due to high computational demand, for completeness we also evaluate our model on single-scene recovery, in line with DPESFM [31]. In this setting, the model is “trained” as usual, with the Adam optimizer and the reprojection error loss function with normalized gradients and hinge loss, but on a single scene. This is indeed very similar to bundle adjustment but with a different parameterization. Interestingly, however, Moran et al. [31] found that even with the direct parameterization with free variables for poses and scene points, these modifications to loss function and optimizer alone can result in much better convergence properties than conventional bundle adjustment, when starting from a random initialization. To a large extent, this is probably explained by the presence of the hinge loss to overcome the depth barrier in case of scene points with negative depths.

For these experiments, we have used a slightly shallower model, with $L = 9$ rather than 12 layers, but the feature dimensions and architecture as a whole remain the same. The model is optimized for 100k iterations. Again, warmup is applied by linearly increasing the learning rate from 0 to $1e-4$ during the first 2500 iterations, followed by an exponential decay corresponding to a factor of 10 every 35k epochs. Figure 10 shows the

resulting average reprojection errors in pixels, compared both with DPESFM [31] as well as other baseline methods reported by [31], i.e. Colmap [36–38], GESFM [24], and Linear [19]. While in many cases our resulting solution has high precision, there are also quite a few failure cases, which are probably cases of suboptimal local reprojection error minima, which interestingly appears to happen more frequently in the single-scene scenario. One possibility is that adding more scenes is effectively flattening the loss landscape, although this should be regarded as nothing more than speculation. In any case, we conclude that our model is more easily trained on multiple scenes simultaneously, in which case we suppose more general geometrical reasoning is encouraged and exploited, and for which our quite expressive model has its edge. Even if we would achieve better performance, it should be noted that Colmap works very well, and is much faster to execute than training a model from scratch, albeit not as fast as our learned model combined with bundle adjustment. In Tables 11 and 12, the corresponding rotation and translation errors are reported. Finally, Table 13 shows corresponding results for the projective setting, in which case the results of all baseline methods are again taken as reported by [31].

	Inference		Inference + BA		Fine-tune		Fine-tune + BA		Colmap	
	Ours	DPESFM	Ours	DPESFM	Ours	DPESFM	Ours	DPESFM		
Reprojection error (px)	Alcatraz Courtyard	36.01	92.37	0.81	0.92	2.83	4.33	0.81	0.81	0.81
	Alcatraz Water Tower	87.67	2831.94	0.88	10.16	8.65	20.66	0.55	0.92	0.55
	Drinking Fountain Somewhere in Zurich	219.75	234.90	0.31	6.73	0.91	11.40	0.31	6.72	0.31
	Nijo Castle Gate	61.41	68.19	0.88	0.89	3.58	4.89	0.73	0.73	0.73
	Porta San Donato Bologna	52.15	84.46	0.76	0.75	4.53	8.01	0.74	0.74	0.75
	Round Church Cambridge	29.80	59.54	0.39	1.49	3.23	5.19	0.39	1.54	0.39
	Smolny Cathedral St Petersburg	85.38	87.81	0.81	0.81	2.51	3.98	0.81	0.81	0.81
	Some Cathedral in Barcelona	125.68	687.83	0.89	16.77	15.73	29.11	0.89	1.91	0.89
	Sri Veeramakaliamman Singapore	83.50	166.68	2.13	9.30	23.41	43.33	0.80	4.29	0.71
	Yueh Hai Ching Temple Singapore	25.60	51.35	0.65	0.73	3.15	8.56	0.65	0.65	0.65
Average	80.69	436.51	0.85	4.86	6.85	13.95	0.67	1.91	0.66	
Rotation error (deg)	Alcatraz Courtyard	6.093	10.946	0.038	0.030	2.293	1.334	0.038	0.035	0.043
	Alcatraz Water Tower	11.501	10.641	0.699	19.351	3.895	5.977	0.227	0.668	0.228
	Drinking Fountain Somewhere in Zurich	15.415	15.704	0.001	22.759	0.488	21.769	0.001	22.747	0.007
	Nijo Castle Gate	17.347	20.032	0.038	0.036	1.036	4.537	0.064	0.063	0.064
	Porta San Donato Bologna	18.411	25.004	0.094	0.094	2.204	6.078	0.097	0.094	0.099
	Round Church Cambridge	10.295	18.685	0.029	1.086	4.827	3.794	0.030	1.158	0.035
	Smolny Cathedral St Petersburg	11.662	14.380	0.023	0.019	2.010	1.170	0.023	0.022	0.029
	Some Cathedral in Barcelona	27.908	29.119	0.020	47.892	16.149	24.625	0.019	1.762	0.025
	Sri Veeramakaliamman Singapore	23.702	36.176	0.457	2.759	9.378	33.969	0.165	1.035	0.169
	Yueh Hai Ching Temple Singapore	9.515	21.561	0.038	0.038	4.103	5.770	0.038	0.038	0.043
Average	15.185	20.225	0.144	9.406	4.638	10.902	0.070	2.762	0.074	
Translation error (m)	Alcatraz Courtyard	2.73	5.74	0.01	0.01	0.60	0.42	0.01	0.01	0.01
	Alcatraz Water Tower	7.53	7.77	0.41	9.05	2.19	3.33	0.12	0.40	0.12
	Drinking Fountain Somewhere in Zurich	4.45	4.46	0.00	1.38	0.08	1.78	0.00	1.38	0.00
	Nijo Castle Gate	5.67	6.95	0.01	0.01	0.30	1.01	0.01	0.01	0.01
	Porta San Donato Bologna	4.80	10.48	0.05	0.05	0.63	1.16	0.05	0.05	0.05
	Round Church Cambridge	5.28	9.00	0.01	0.56	1.47	1.48	0.01	0.59	0.01
	Smolny Cathedral St Petersburg	2.33	2.52	0.01	0.01	0.11	0.17	0.01	0.01	0.01
	Some Cathedral in Barcelona	12.32	12.66	0.01	11.93	6.67	9.82	0.01	0.62	0.01
	Sri Veeramakaliamman Singapore	4.93	4.90	0.14	0.77	2.28	4.83	0.04	0.29	0.04
	Yueh Hai Ching Temple Singapore	2.44	4.28	0.01	0.01	0.49	1.32	0.01	0.01	0.01
Average	5.25	6.88	0.07	2.38	1.48	2.53	0.03	0.34	0.03	

Table 7. Euclidean reconstruction of novel test scenes, with model trained with data augmentation. The results of DPESFM [31] have been acquired by us training the model. The result of Colmap, as reported by [31], is also added for reference.

	Inference		Inference + BA		Fine-tune		Fine-tune + BA		VarPro
	Ours	DPESFM	Ours	DPESFM	Ours	DPESFM	Ours	DPESFM	
Alcatraz Water Tower	100.16	80.94	1.71	3.86 (7.37)	3.48	9.83	0.47	0.99 (0.47)	0.47
Dinosaur 319	72.80	15.73	1.63	1.22 (1.58)	38.98	3.84	5.88	1.32 (1.30)	0.43
Dinosaur 4983	61.54	24.89	1.23	1.10 (3.99)	4.83	4.49	0.64	0.92 (1.14)	0.42
Drinking Fountain Somewhere in Zurich	136.73	238.87	0.28	0.28 (14.39)	0.64	2.18	0.28	0.28 (0.28)	0.28
Eglise Du Dome	60.29	51.72	2.49	1.15 (2.10)	4.66	7.26	0.45	0.29 (1.27)	-
Gustav Vasa	195.08	525.96	1.63	1.62 (6.30)	1.59	3.12	0.16	0.16 (0.16)	0.16
Nijo Castle Gate	98.42	80.07	0.40	0.41 (3.27)	125.86	4.11	2.57	0.39 (0.39)	0.39
Skansen Kronan Gothenburg	51.23	38.77	0.48	0.70 (1.64)	3.42	2.74	0.41	0.41 (0.41)	-
Some Cathedral in Barcelona	452.21	139.54	1.68	1.08 (14.87)	15.35	17.23	1.51	1.67 (0.51)	-
Sri Veeramakaliamman Singapore	247.45	165.56	4.40	5.42 (18.25)	190.05	41.00	4.02	3.85 (5.45)	-
Average	147.59	136.21	1.59	1.68 (7.38)	38.89	9.58	1.64	1.03 (1.14)	-

Table 8. Reprojection errors of projective reconstruction of novel test scenes, with model trained without data augmentation. The results of DPESFM [31] have been acquired by us training the model, along with the results reported by [31] in parentheses, if available. The result of VarPro, as reported by [31], is also added for reference.

D.4. Visualizations of Novel Scene Reconstructions

In Figures 6-15, we provide visualizations for the Euclidean reconstructions of all 10 novel test scenes, corresponding to the results reported in Sections 4.2 and 4.3, both for our model as well as DPESFM [31]. All point clouds are predictions, together with estimated (red) and ground truth (blue) camera poses. Some outlier filtering has been carried out on the plotted point clouds by coordinate-wise quantiles. Again, please note that the ground truth poses are aligned with the predicted cam-

eras according to Section C, and as such their relative motion is only meaningful if the predicted poses are good enough for the alignment to be accurately estimated (typically after BA but not always before). It can be observed from the plots that our method combined with BA can typically recover high quality scene structures and camera poses, especially when combined with data augmentation. While DPESFM [31] combined with BA also often works relatively well, one notable failure case is *Sri Veeramakaliamman Singapore*, which is a very large scene, that we however manage to recover

Scene	Infer.	BA	GPSFM
Alcatraz Water Tower	0.12	84.67	137.06
Dinosaur 319	0.07	1.43	3.25
Dinosaur 4983	0.07	6.11	4.99
Eglise Du Dome	0.42	70.91	105.84
Drinking Fountain Somewhere in Zurich	0.07	3.48	3.35
Gustav Vasa	0.08	4.46	3.45
Nijo Castle Gate	0.13	5.89	6.37
Skansen Kronan Gothenburg	0.27	89.31	93.83
Some Cathedral in Barcelona	0.25	91.21	110.49
Sri Veeramakaliamman Singapore	0.63	133.43	301.71

Table 9. Runtime (s) of our model for projective reconstruction on test scenes, in comparison with VarPro (measured by [31]).

quite descently. Also note that while our results are in general improved by incorporating data augmentation, it is quite noticeable that DPESFM breaks down from this, possibly due to a limited model capacity / expressivity. In particular, with the help of data augmentation, we are able to recover the *Some Cathedral in Barcelona* scene very well, while DPESFM still fails, and in general shows deteriorated results whenever data augmentation is applied.

	Before BA				After BA				Colmap
	Ours	DPESFM	GESFM	Linear	Ours	DPESFM	GESFM	Linear	
Alcatraz Courtyard	0.98	1.64	66.5	16.58	0.81	0.81	4.67	1.27	0.81
Alcatraz Water Tower	1.69	2.13	131.81	56.26	0.93	0.55	25.93	73.72	0.55
Buddah Tooth Relic Temple Singapore	1.73	2.06	89.94	47.5	0.85	0.85	13.22	2.66	0.85
Doge Palace Venice	1.28	3.62	123.53	-	0.98	1.00	22.32	-	0.98
Door Lund	11.50	0.32	(227.0)	20.89	9.94	0.30	(9.21)	0.30	0.30
Drinking Fountain Somewhere in Zurich	0.36	0.33	(0.94)	0.58	0.31	0.31	(0.27)	0.31	0.31
East Indiaman Goteborg	1.40	4.13	170.63	(94.46)	0.89	1.85	32.37	(312.9)	0.89
Ecole Superior De Guerre	0.54	0.72	(0.35)	1.48	0.34	0.34	(0.14)	0.34	0.34
Eglise Du Dome	0.63	0.91	(90.83)	26.4	0.27	0.27	(6.21)	0.76	0.27
Folke Filbyter	41.44	10.37	(5.74)	72.06	11.11	4.29	(0.41)	6.06	0.29
Fort Channing Gate Singapore	0.29	0.52	2.57	22.69	0.25	0.25	0.25	0.45	0.25
Golden Statue Somewhere in Hong Kong	0.49	0.40	4.98	73.7	0.27	0.27	0.27	0.3	0.27
Gustav II Adolf	15.31	13.91	6.49	31.08	11.71	11.49	0.26	0.26	0.26
Gustav Vasa	3.72	3.52	(5.21)	11.99	3.15	3.15	(0.31)	0.48	0.48
Jonas Ahlstromer	10.09	10.82	(36.48)	236.41	7.25	8.41	(0.69)	4.69	0.22
King 's College University of Toronto	0.55	0.90	(11.87)	(27.29)	0.34	0.34	(0.35)	(7.12)	0.34
Lund University Sphinx	0.75	4.78	7.19	60.64	0.39	1.36	0.4	4.58	0.39
Nijo Castle Gate	1.69	1.70	11.18	154.96	0.73	0.73	0.73	4.84	0.73
Pantheon Paris	0.65	1.47	79.24	39.69	0.49	0.49	9.71	0.82	-
Park Gate Clermont Ferrand	7.71	0.57	1.71	10.5	6.75	0.35	0.35	0.35	0.35
Plaza De Armas Santiago	7.36	7.40	146.56	-	4.75	4.90	15.61	-	1.13
Porta San Donato Bologna	1.12	2.28	29.5	46.12	0.74	0.75	3.23	1.16	0.75
Round Church Cambridge	2.52	2.66	19.04	9.6	1.50	1.54	2.03	0.41	0.39
Skansen Kronan Gothenburg	0.74	1.24	8.82	(18.49)	0.67	0.67	0.67	(0.69)	0.67
Smolny Cathedral St Petersburg	0.93	1.66	19.01	-	0.81	0.81	1.0	-	0.81
Some Cathedral in Barcelona	1.04	2.87	47.12	66.97	0.89	0.89	1.09	2.09	0.89
Sri Mariamman Singapore	1.36	4.13	52.13	37.16	0.89	0.91	7.4	1.17	0.89
Sri Thendayuthapani Singapore	0.87	23.37	(15.93)	19.57	0.67	8.44	(0.56)	0.72	0.67
Sri Veeramakaliamman Singapore	2.00	3.47	(205.96)	18.08	0.71	0.73	(34.72)	2.2	0.71
Statue Of Liberty	113.76	26.16	(1031.8)	133.81	32.51	6.97	(52.05)	5.08	1.25
The Pumpkin	13.07	33.41	9.71	(122.54)	8.67	24.85	0.57	(24.19)	0.57
Thian Hook Keng Temple Singapore	5.18	2.75	53.79	62.7	1.87	1.13	3.32	4.92	1.12
Tsar Nikolai I	15.40	9.79	5.19	32.86	10.48	6.53	0.33	0.33	0.33
Urban II	17.58	9.38	31.71	176.19	12.70	6.92	0.72	17.61	0.38
Vercingetorix	6.96	5.08	15.87	65.57	5.02	1.50	0.54	2.93	0.23
Yueh Hai Ching Temple Singapore	0.87	0.94	(27.32)	45.19	0.65	0.65	(1.64)	2.06	0.65

Table 10. Results of single-scene recovery of Euclidean scenes (average reprojection errors in pixels), compared with DPESFM [31], GESFM [24], Linear [19], and Colmap [36–38]. Parentheses mark scenes for which a baseline method has disregarded at least 10% of the cameras.

	Before BA				After BA				Colmap
	Ours	DPESFM	GESFM	Linear	Ours	DPESFM	GESFM	Linear	
Alcatraz Courtyard	0.424	0.619	1.851	0.729	0.038	0.049	0.533	0.042	0.043
Alcatraz Water Tower	1.763	0.933	1.136	1.525	0.677	0.230	9.997	1.525	0.228
Buddah Tooth Relic Temple Singapore	1.545	1.030	2.95	2.058	0.081	0.081	4.709	0.551	0.083
Doge Palace Venice	0.345	1.163	2.75	-	0.048	0.211	5.317	-	0.031
Door Lund	13.940	0.024	(2.041)	1.148	12.844	0.006	(7.552)	0.005	0.005
Drinking Fountain Somewhere in Zurich	0.119	0.031	(0.054)	0.077	0.001	0.007	(0.01)	0.007	0.007
East Indiaman Goteborg	1.426	3.814	11.129	(3.284)	0.251	3.117	12.396	(3.284)	0.251
Ecole Superior De Guerre	0.243	0.318	(0.057)	0.182	0.018	0.024	(0.035)	0.024	0.024
Eglise Du Dome	0.801	0.808	(2.851)	0.903	0.031	0.037	(3.631)	0.162	0.036
Folke Filbyter	74.307	74.596	(0.332)	1.94	68.096	70.157	(0.148)	4.484	0.036
Fort Channing Gate Singapore	0.063	0.207	0.295	0.659	0.010	0.020	0.02	0.029	0.020
Golden Statue Somewhere in Hong Kong	0.692	0.292	0.669	8.264	0.024	0.031	0.03	0.022	0.031
Gustav II Adolf	88.777	67.784	0.435	1.398	66.266	58.458	0.021	0.021	0.021
Gustav Vasa	39.767	34.181	(0.841)	1.658	32.316	32.266	(0.751)	0.839	0.841
Jonas Ahlstromer	44.994	50.190	(1.994)	10.154	49.640	47.117	(0.082)	5.391	0.036
King 's College University of Toronto	1.097	0.989	(0.645)	(1.07)	0.083	0.085	(0.059)	(4.624)	0.084
Lund University Sphinx	0.806	19.522	0.738	3.476	0.025	8.752	0.058	5.452	0.033
Nijo Castle Gate	0.959	1.495	0.399	2.097	0.064	0.069	0.064	0.744	0.064
Pantheon Paris	0.334	0.192	3.766	2.655	0.038	0.040	3.208	0.072	-
Park Gate Clermont Ferrand	25.295	0.391	0.203	0.296	24.779	0.049	0.049	0.049	0.049
Plaza De Armas Santiago	5.964	6.782	6.291	-	2.299	2.556	6.344	-	0.122
Porta San Donato Bologna	0.377	2.153	1.013	1.381	0.093	0.095	0.513	0.149	0.099
Round Church Cambridge	2.182	2.451	1.021	0.634	1.099	1.107	1.851	0.033	0.035
Skansen Kronan Gothenburg	0.235	0.736	0.549	(0.679)	0.017	0.026	0.025	(0.02)	0.025
Smolny Cathedral St Petersburg	0.469	0.554	0.493	-	0.023	0.033	0.028	-	0.029
Some Cathedral in Barcelona	0.180	0.880	1.519	3.126	0.019	0.026	0.031	0.057	0.025
Sri Mariamman Singapore	1.003	2.302	1.433	1.615	0.075	0.077	2.158	0.083	0.078
Sri Thendayuthapani Singapore	0.835	46.269	(1.561)	1.581	0.137	44.170	(0.329)	0.138	0.138
Sri Veeramakaliamman Singapore	1.876	2.559	(1.807)	0.519	0.167	0.175	(3.41)	0.288	0.169
Statue Of Liberty	75.495	46.887	(3.449)	3.357	73.142	9.091	(8.281)	2.945	0.213
The Pumpkin	12.650	94.672	2.036	(4.215)	9.136	98.862	0.092	(3.123)	0.091
Thian Hook Keng Temple Singapore	3.691	0.832	2.751	3.047	0.386	0.081	0.245	0.424	0.084
Tsar Nikolai I	72.322	48.499	0.475	1.437	74.349	36.280	0.018	0.018	0.018
Urban II	60.201	47.490	2.077	8.951	59.713	48.214	0.175	16.348	0.107
Vercingetorix	91.624	69.328	2.203	2.365	82.565	17.706	1.431	7.138	0.048
Yueh Hai Ching Temple Singapore	0.752	0.720	(1.813)	1.92	0.038	0.043	(0.075)	0.26	0.043

Table 11. Results of single-scene recovery of Euclidean scenes (rotation errors in degrees), compared with DPESFM [31], GESFM [24], Linear [19], and Colmap [36–38]. Parentheses mark scenes for which a baseline method has disregarded at least 10% of the cameras.

	Before BA				After BA				
	Ours	DPESFM	GESFM	Linear	Ours	DPESFM	GESFM	Linear	Colmap
Alcatraz Courtyard	0.103	0.160	0.767	0.378	0.014	0.015	0.259	0.014	0.014
Alcatraz Water Tower	1.088	0.518	8.332	1.643	0.393	0.116	9.147	1.643	0.115
Buddah Tooth Relic Temple Singapore	0.313	0.233	2.124	1.325	0.015	0.014	1.429	0.125	0.015
Doge Palace Venice	0.084	0.342	1.688	-	0.014	0.029	1.608	-	0.012
Door Lund	1.009	0.006	(1.603)	0.226	1.386	0.001	(0.973)	0.001	0.001
Drinking Fountain Somewhere in Zurich	0.012	0.004	(0.016)	0.024	0.002	0.002	(0.002)	0.002	0.002
East Indiaman Goteborg	0.348	0.621	2.783	(2.235)	0.065	0.509	3.099	(2.235)	0.065
Ecole Superior De Guerre	0.066	0.081	(0.006)	0.048	0.005	0.005	(0.002)	0.005	0.005
Eglise Du Dome	0.212	0.205	(1.958)	0.128	0.010	0.010	(1.425)	0.046	0.010
Folke Filbyter	0.123	0.125	(0.003)	0.021	0.110	0.118	(0.000)	0.123	0.000
Fort Channing Gate Singapore	0.027	0.093	0.092	0.139	0.00008	0.008	0.008	0.013	0.008
Golden Statue Somewhere in Hong Kong	0.120	0.073	0.118	1.153	0.004	0.004	0.004	0.004	0.004
Gustav II Adolf	13.324	9.714	0.134	0.333	9.717	8.524	0.004	0.004	0.004
Gustav Vasa	1.235	1.085	(0.079)	0.266	1.136	1.145	(0.101)	0.099	0.1
Jonas Ahlstromer	8.649	10.888	(0.35)	0.895	10.405	10.451	(0.01)	1.259	0.011
King 's College University of Toronto	0.159	0.235	(0.152)	(1.781)	0.017	0.017	(0.005)	(1.877)	0.017
Lund University Sphinx	0.218	4.585	0.228	1.199	0.009	2.191	0.016	1.512	0.009
Nijo Castle Gate	0.195	0.286	0.141	0.348	0.011	0.012	0.011	0.19	0.011
Pantheon Paris	0.029	0.050	0.867	1.275	0.005	0.005	0.595	0.011	-
Park Gate Clermont Ferrand	11.706	0.125	0.083	0.1	11.391	0.022	0.022	0.022	0.022
Plaza De Armas Santiago	2.634	2.944	2.45	-	1.252	1.383	2.244	-	0.048
Porta San Donato Bologna	0.097	0.388	0.949	1.588	0.046	0.046	0.169	0.067	0.047
Round Church Cambridge	0.926	1.003	0.486	0.217	0.570	0.582	0.493	0.012	0.012
Skansen Kronan Gothenburg	0.071	0.226	0.223	(0.234)	0.008	0.008	0.008	(0.007)	0.008
Smolny Cathedral St Petersburg	0.021	0.051	0.209	-	0.006	0.006	0.007	-	0.006
Some Cathedral in Barcelona	0.063	0.315	1.776	1.261	0.011	0.011	0.013	0.024	0.010
Sri Mariamman Singapore	0.244	0.683	1.758	0.721	0.023	0.023	0.614	0.025	0.023
Sri Thendayuthapani Singapore	0.154	3.812	(0.285)	0.375	0.034	2.870	(0.053)	0.034	0.034
Sri Veeramakaliamman Singapore	0.432	0.597	(1.966)	0.273	0.038	0.040	(1.388)	0.095	0.038
Statue Of Liberty	27.130	20.012	(4.55)	3.031	28.350	4.122	(4.782)	28.049	0.099
The Pumpkin	2.881	14.890	0.513	(1.656)	2.223	14.952	0.022	(14.862)	0.022
Thian Hook Keng Temple Singapore	0.450	0.082	0.519	0.404	0.055	0.008	0.024	0.043	0.008
Tsar Nikolai I	12.843	9.467	0.219	0.261	13.990	7.836	0.005	0.005	0.005
Urban II	11.350	9.467	0.774	2.044	10.882	9.586	0.036	3.038	0.021
Vercingetorix	11.202	8.788	1.158	2.786	9.696	3.104	0.3	1.564	0.011
Yueh Hai Ching Temple Singapore	0.099	0.098	(0.642)	0.303	0.014	0.014	(0.023)	0.059	0.014

Table 12. Results of single-scene recovery of Euclidean scenes (translation errors in meters), compared with DPESFM [31], GESFM [24], Linear [19], and Colmap [36–38]. Parentheses mark scenes for which a baseline method has disregarded at least 10% of the cameras.

	Before BA			After BA				VarPro
	Ours	DPESFM	GPSFM	Ours	DPESFM	GPSFM	PPSFM	
Alcatraz Courtyard	0.77	1.55	20.34	0.51	0.52	0.52	0.57	0.52
Alcatraz Water Tower	1.00	2.18	16.50	0.47	0.47	0.63	0.59	0.47
Alcatraz West Side Gardens	1.27	9.54	1007.50	0.72	0.76	326.99	1.77	-
Basilica Di San Petronio	6.78	7.90	1871.41	1.14	0.96	60.69	0.63	-
Buddah Statue	418.74	18.88	919.26	7.73	2.93	96.96	0.41	-
Buddah Tooth Relic Temple Singapore	1.77	4.59	18.53	0.59	0.60	0.62	0.71	0.60
Corridor	0.32	0.30	0.64	0.26	0.26	0.26	0.27	0.26
Dinosaur 319	1.25	2.35	4.66	0.93	1.53	0.43	0.47	0.43
Dinosaur 4983	4.99	1.96	1.54	0.95	0.57	0.42	0.47	0.42
Doge Palace Venice	1.45	3.60	170.93	0.60	0.60	3.52	0.67	-
Drinking Fountain Somewhere in Zurich	0.32	0.33	1.29	0.28	0.28	0.28	0.31	0.28
East Indiaman Goteborg	27.44	3.31	99.38	3.23	0.99	5.11	0.67	-
Ecole Superior De Guerre	0.56	0.75	1.88	0.26	0.26	0.26	0.28	0.26
Eglise Du Dome	0.95	1.10	8.41	0.23	0.24	0.24	0.25	-
Folke Filbyter	115.59	8.87	1.78	8.76	8.58	0.82	0.33	277.89
Golden Statue Somewhere in Hong Kong	0.56	0.35	0.81	0.22	0.22	0.22	0.24	0.22
Gustav II Adolf	196.68	14.77	5.91	8.10	5.83	0.23	0.24	0.23
Gustav Vasa	0.56	0.23	1.82	0.16	0.16	0.16	0.17	0.16
Jonas Ahlstromer	16.16	14.38	28.83	5.37	4.72	0.18	0.20	0.18
King 's College University of Toronto	2.19	2.27	22.89	0.51	0.78	2.35	0.26	0.24
Lund University Sphinx	81.34	3.64	10.00	0.82	0.34	0.45	0.37	0.34
Model House	0.49	0.37	3.66	0.34	0.34	1.12	0.40	0.34
Nijo Castle Gate	1.21	0.71	20.08	0.39	0.39	0.39	0.43	0.39
Pantheon Paris	0.96	1.75	44.85	0.48	0.49	2.85	0.62	-
Park Gate Clermont Ferrand	0.47	0.61	13.82	0.31	0.31	0.32	0.49	0.31
Plaza De Armas Santiago	2.42	5.10	81.01	0.69	0.64	3.14	0.71	-
Porta San Donato Bologna	0.90	1.58	33.36	0.40	0.40	0.61	3.75	0.40
Skansen Kronan Gothenburg	0.59	1.19	8.90	0.41	0.41	0.44	0.44	-
Skansen Lejonet Gothenburg	8.22	10.82	69.81	1.21	2.05	7.48	1.28	-
Smolny Cathedral St Petersburg	0.55	1.66	83.78	0.46	0.46	0.46	0.50	-
Some Cathedral in Barcelona	0.82	3.67	14.77	0.51	0.51	0.51	0.54	-
Sri Mariamman Singapore	2.39	7.06	39.89	1.02	0.61	0.78	0.85	-
Sri Thendayuthapani Singapore	3.30	2.12	13.25	2.08	0.31	0.56	0.33	-
Sri Veeramakaliamman Singapore	13.80	6.47	99.99	3.98	0.52	1.78	0.66	-
The Pumpkin	3516.42	14.45	8.97	75.77	0.38	0.38	0.42	-
Thian Hook Keng Temple Singapore	7.99	7.59	26.78	0.54	0.54	0.55	0.66	0.54
Tsar Nikolai I	25.75	6.04	13.21	4.03	2.43	0.33	0.31	0.29
Urban II	487.12	16.91	87.25	23.68	6.84	0.27	0.31	3.61

Table 13. Results of single-scene recovery of projective scenes (average reprojection errors in pixels), compared with DPESFM [31], GPSFM [23], and PPSFM [28], and VarPro [16].

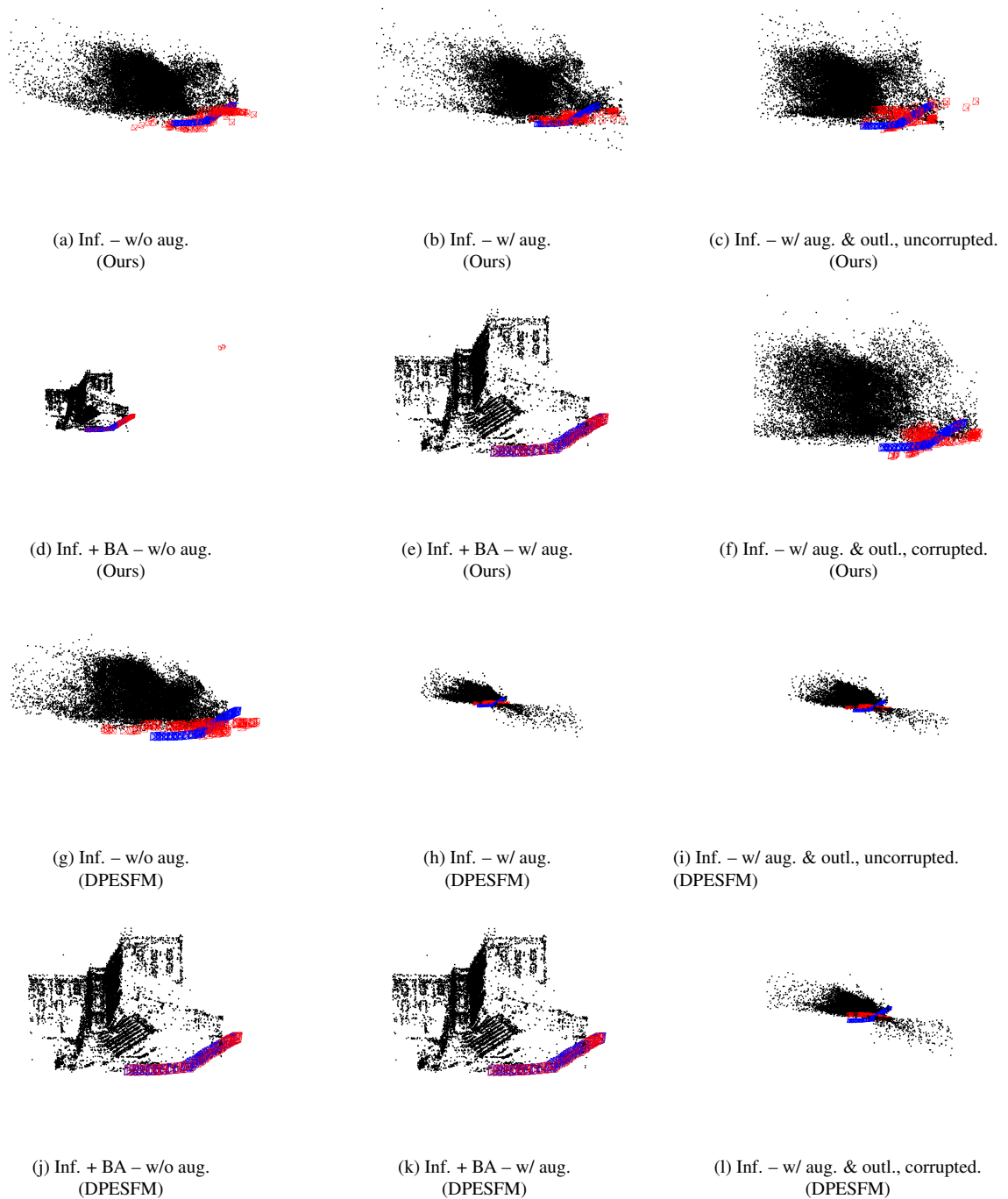


Figure 6. Euclidean reconstruction of *Alcatraz Courtyard*. 6a-6b and 6a-6b show the results of our method with and without data augmentation and bundle adjustment, while 6c and 6f show the results of training with artificially injected outliers, with / without corruption of the test scene as well. Finally, the corresponding results of DPESFM [31] can be seen in 6g-6l.

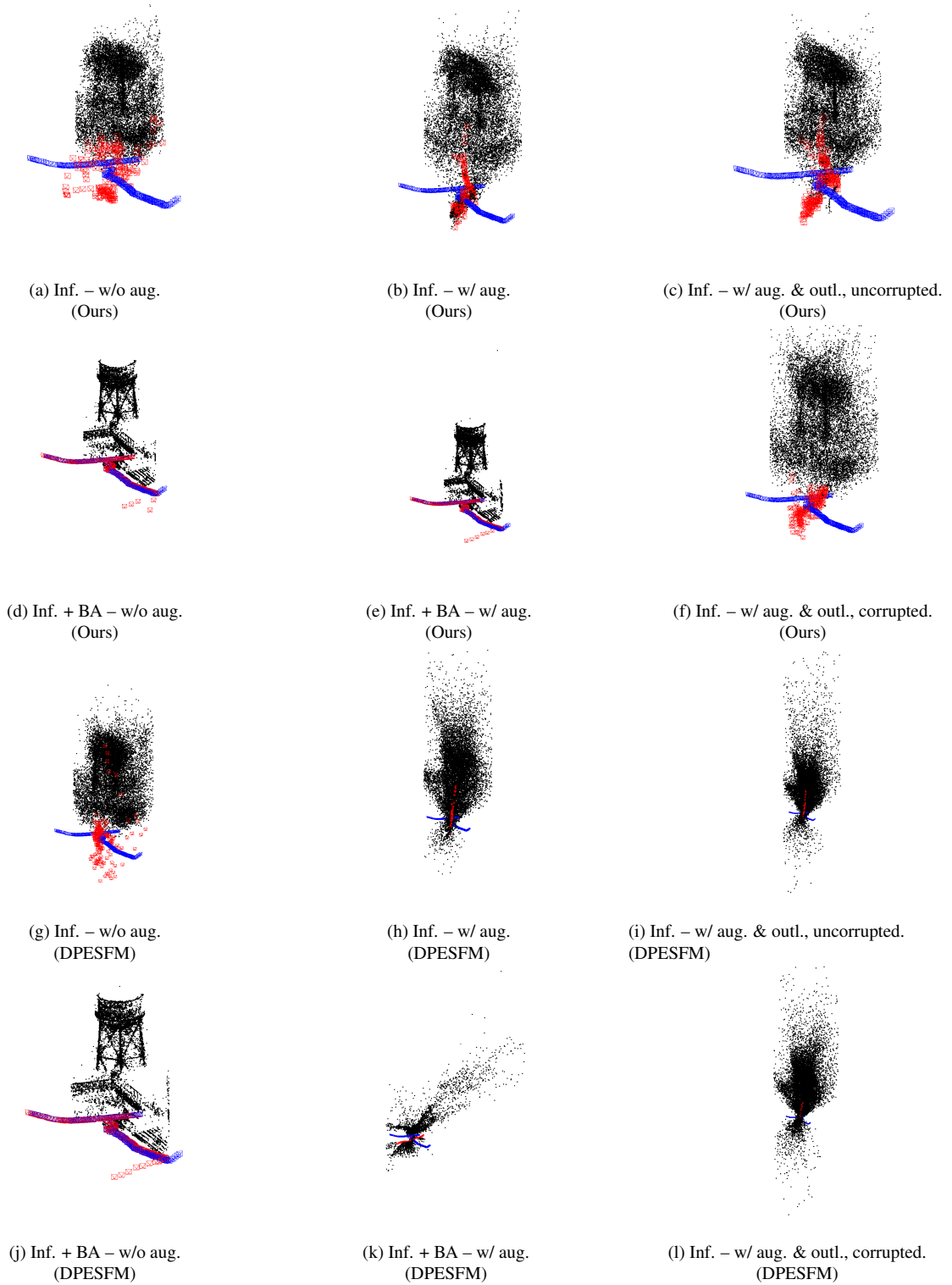


Figure 7. Euclidean reconstruction of *Alcatraz Water Tower*. **7a-7b** and **7a-7b** show the results of our method with and without data augmentation and bundle adjustment, while **7c** and **7f** show the results of training with artificially injected outliers, with / without corruption of the test scene as well. Finally, the corresponding results of DPESFM [31] can be seen in **7g-7l**.

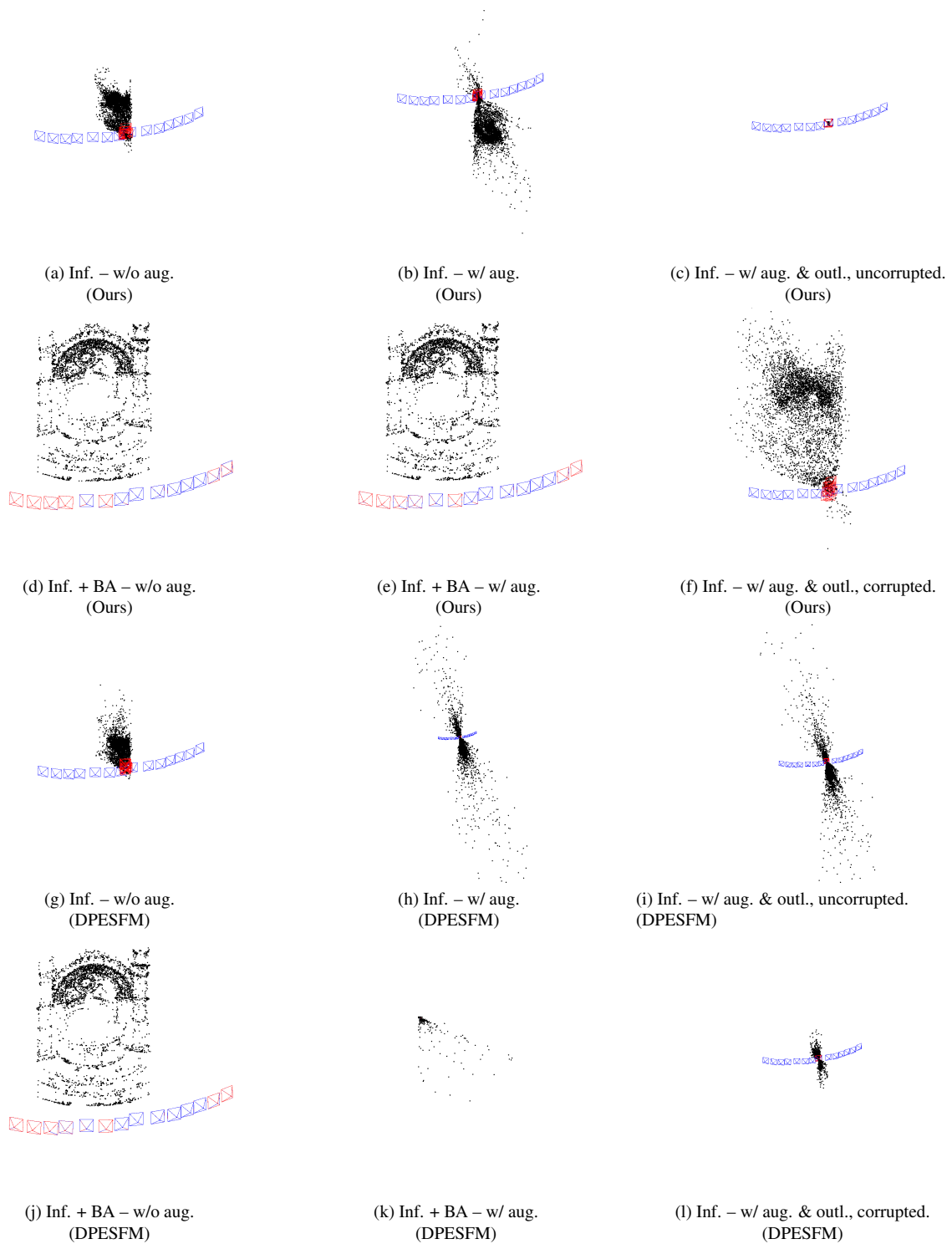


Figure 8. Euclidean reconstruction of *Drinking Fountain Somewhere in Zurich*. 8a-8b and 8a-8b show the results of our method with and without data augmentation and bundle adjustment, while 8c and 8f show the results of training with artificially injected outliers, with / without corruption of the test scene as well. Finally, the corresponding results of DPESFM [31] can be seen in 8g-8l.

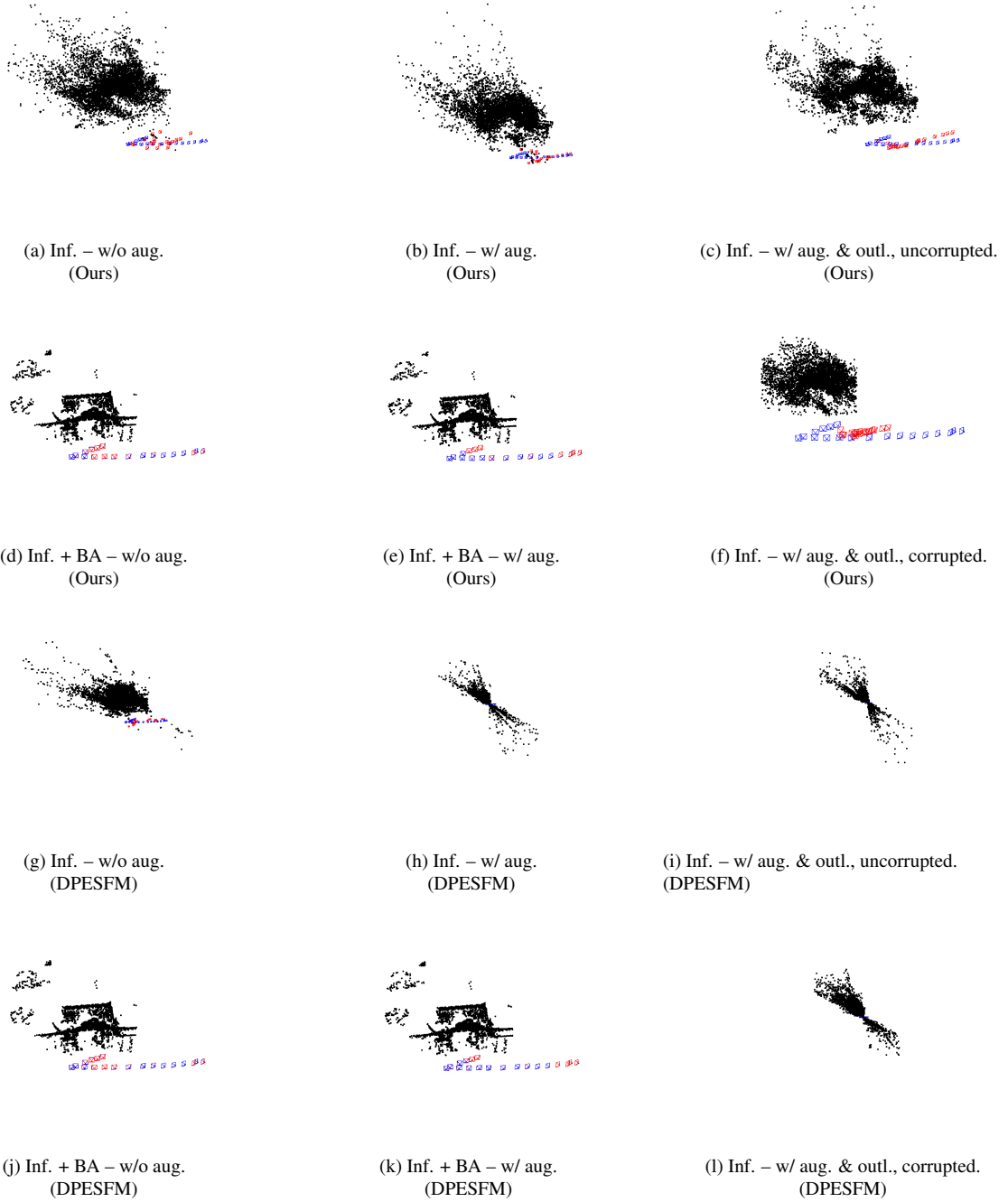


Figure 9. Euclidean reconstruction of *Nijo Castle Gate*. 9a-9b and 9a-9b show the results of our method with and without data augmentation and bundle adjustment, while 9c and 9f show the results of training with artificially injected outliers, with / without corruption of the test scene as well. Finally, the corresponding results of DPESFM [31] can be seen in 9g-9l.

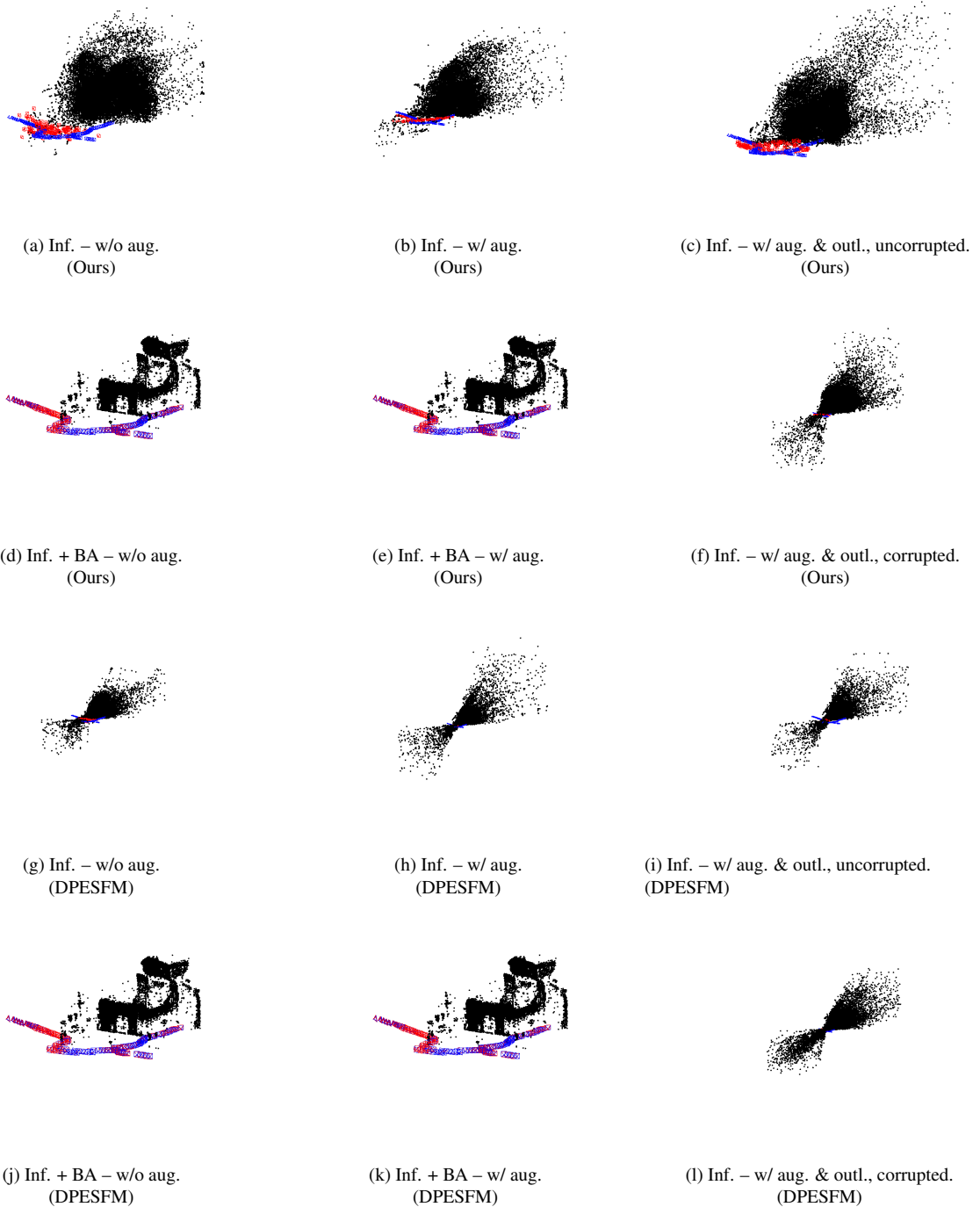


Figure 10. Euclidean reconstruction of *Porta San Donato Bologna*. 10a-10b and 10a-10b show the results of our method with and without data augmentation and bundle adjustment, while 10c and 10f show the results of training with artificially injected outliers, with / without corruption of the test scene as well. Finally, the corresponding results of DPESFM [31] can be seen in 10g-10l.

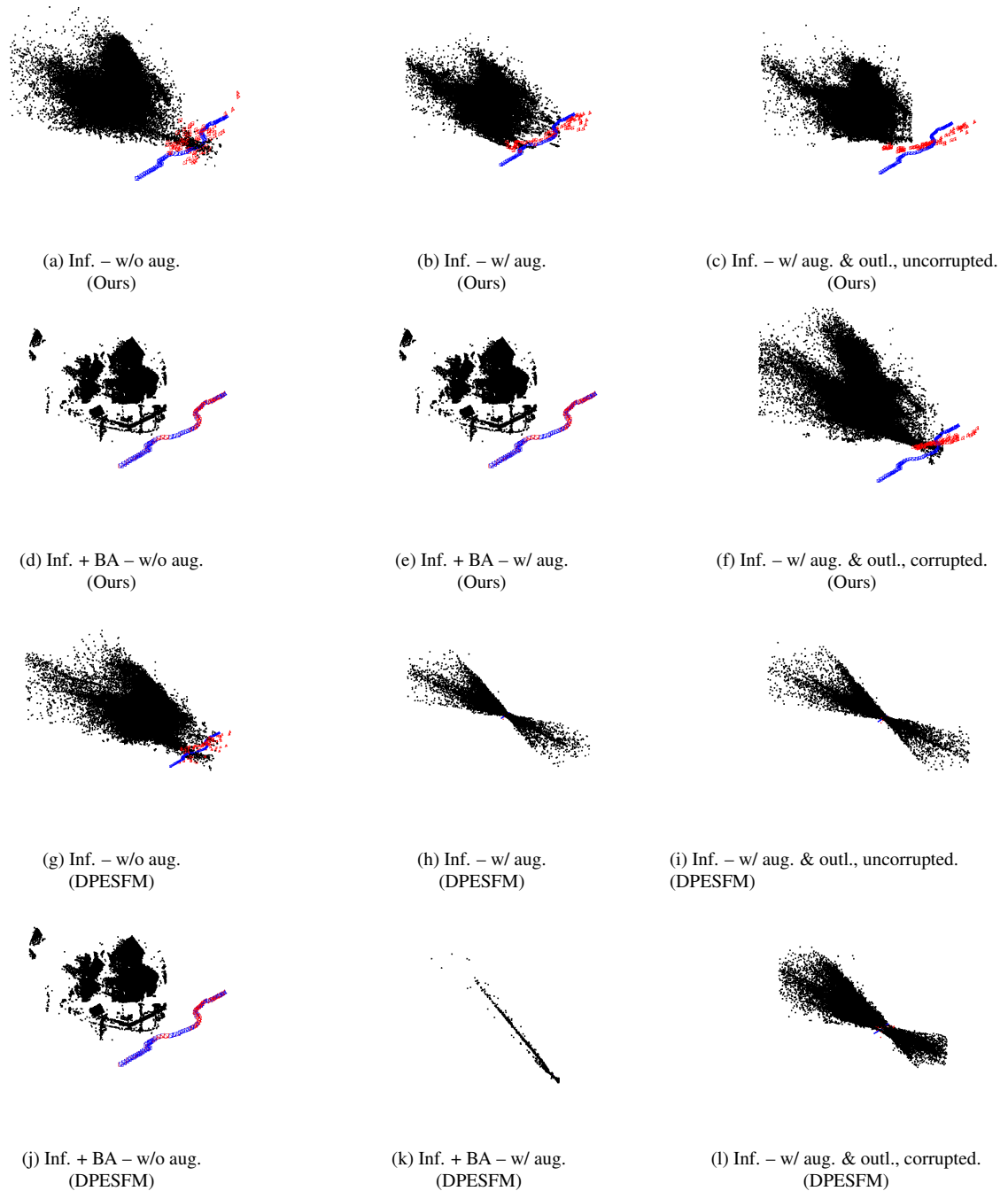


Figure 11. Euclidean reconstruction of *Round Church Cambridge*. **11a-11b** and **11a-11b** show the results of our method with and without data augmentation and bundle adjustment, while **11c** and **11f** show the results of training with artificially injected outliers, with / without corruption of the test scene as well. Finally, the corresponding results of DPESFM [31] can be seen in **11g-11l**.

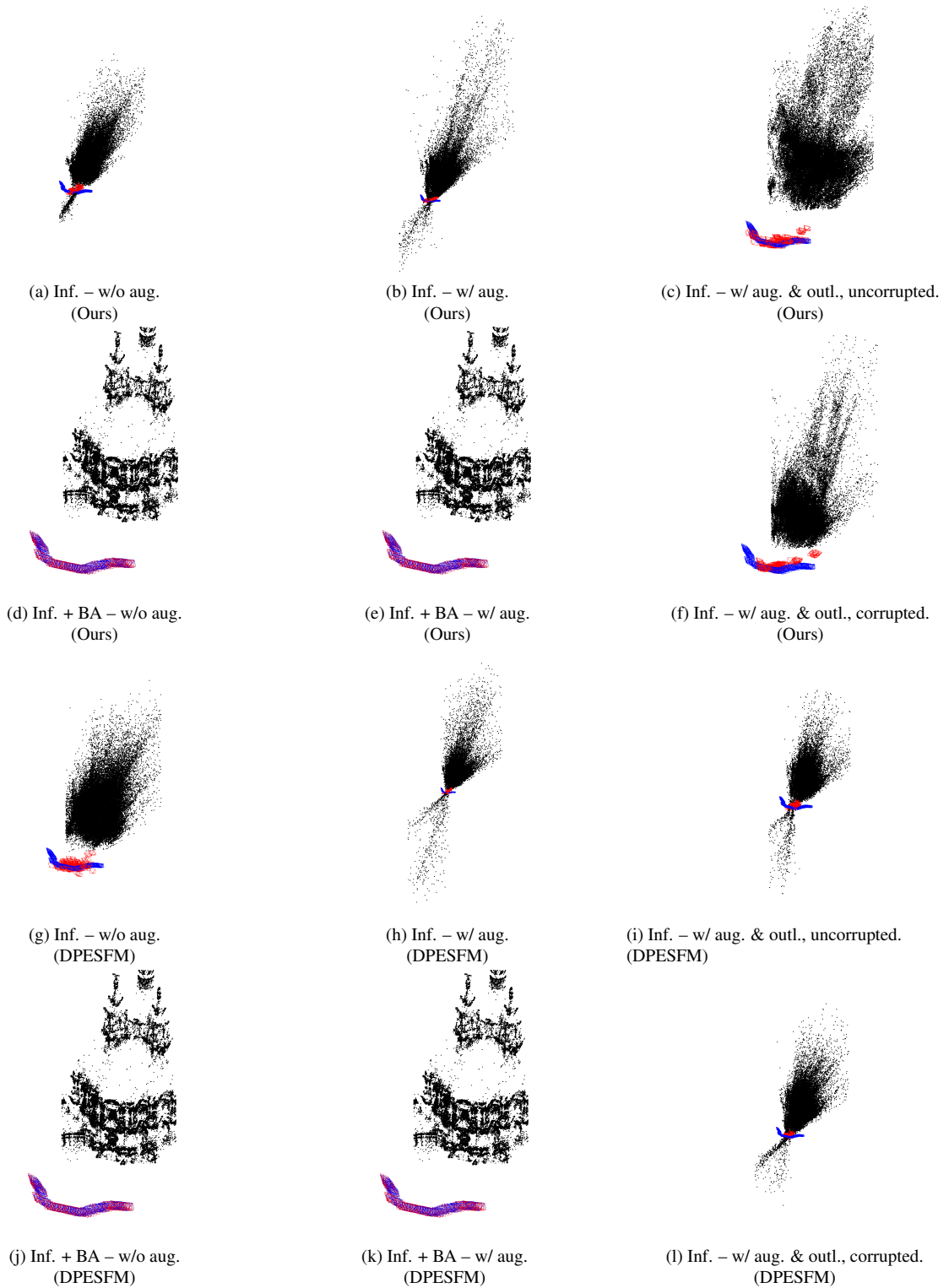


Figure 12. Euclidean reconstruction of *Smolny Cathedral St Petersburg*. 12a-12b and 12a-12b show the results of our method with and without data augmentation and bundle adjustment, while 12c and 12f show the results of training with artificially injected outliers, with / without corruption of the test scene as well. Finally, the corresponding results of DPESFM [31] can be seen in 12g-12l.

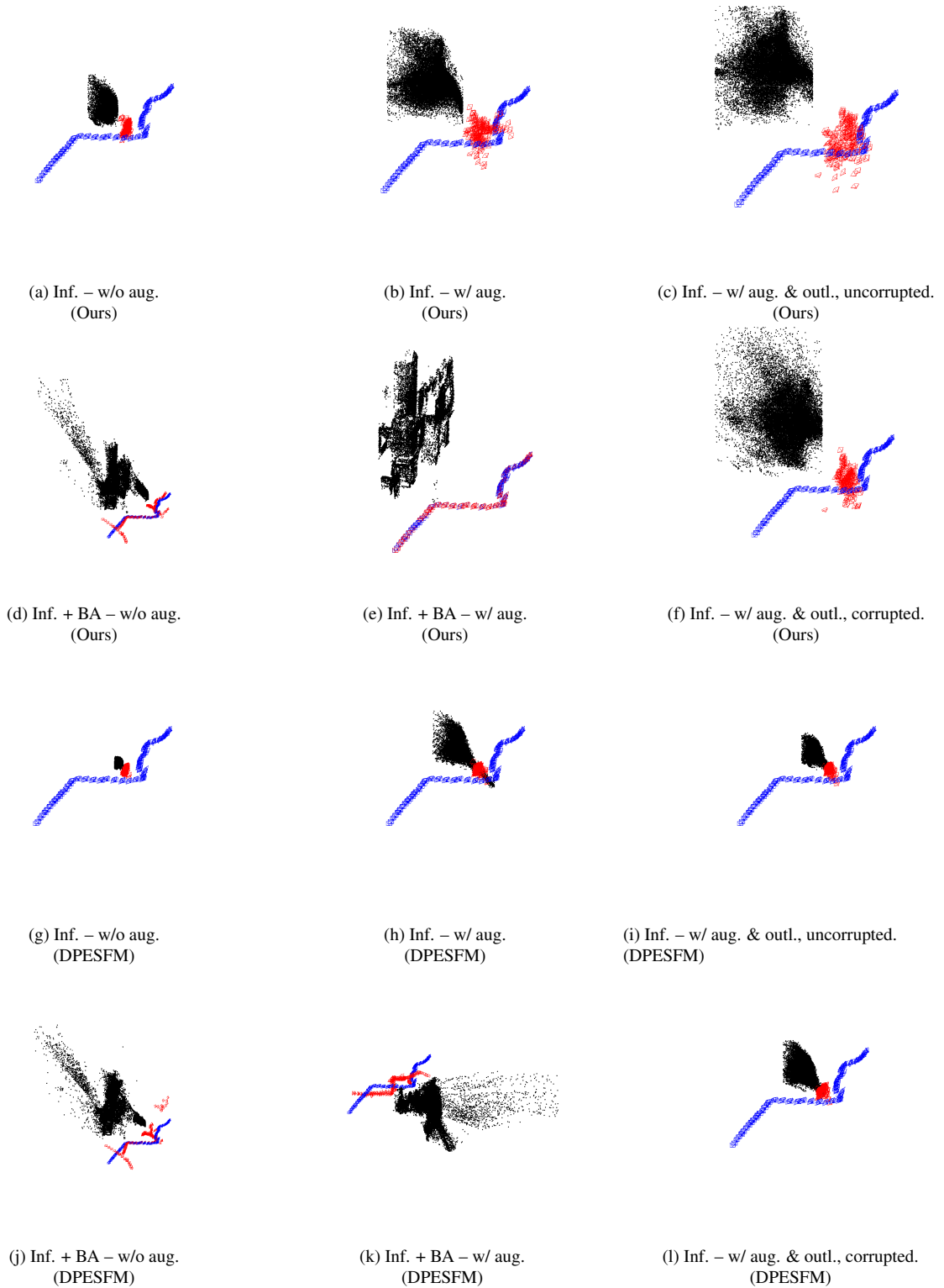


Figure 13. Euclidean reconstruction of *Some Cathedral in Barcelona*. 13a-13b and 13a-13b show the results of our method with and without data augmentation and bundle adjustment, while 13c and 13f show the results of training with artificially injected outliers, with / without corruption of the test scene as well. Finally, the corresponding results of DPESFM [31] can be seen in 13g-13l.

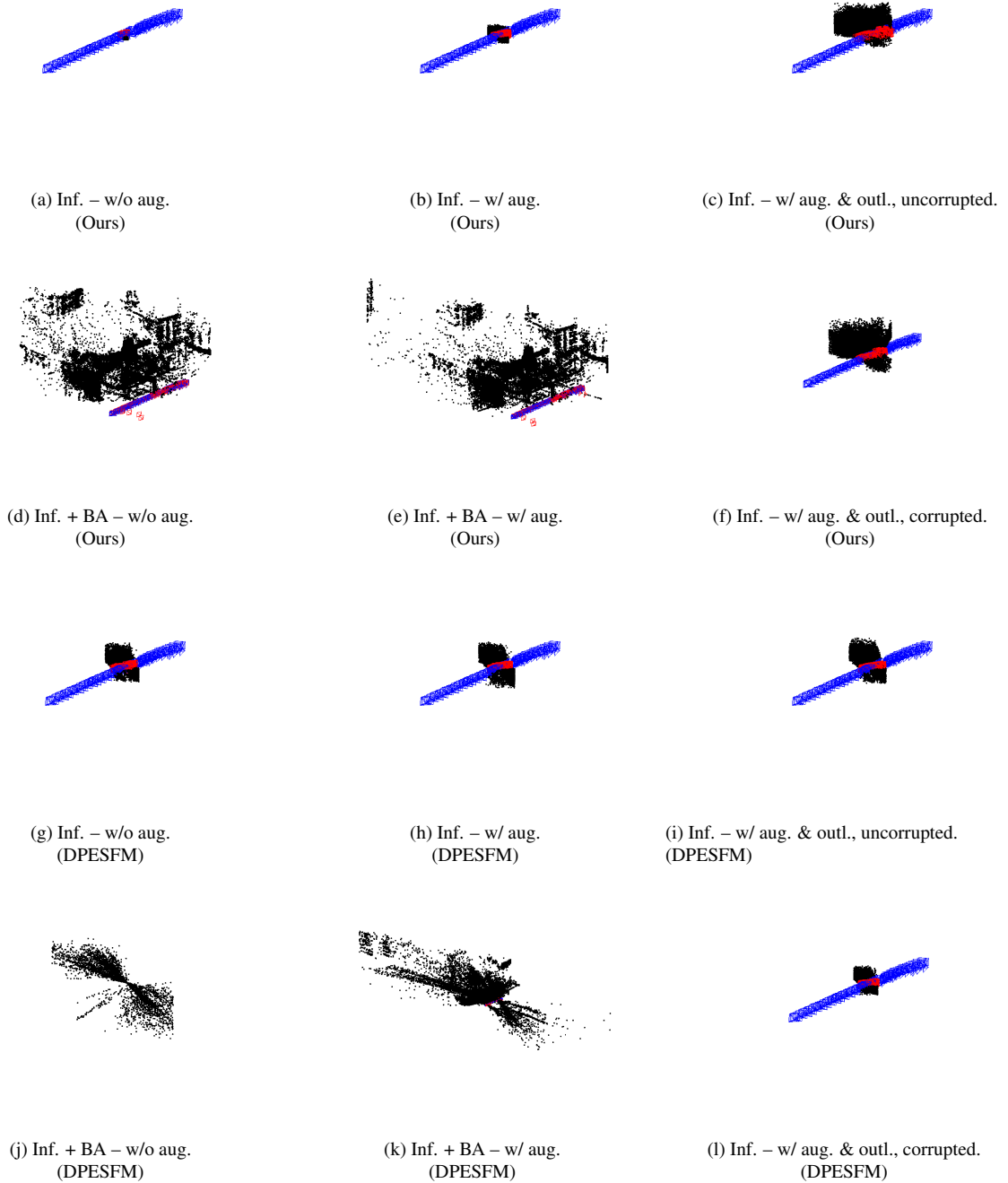


Figure 14. Euclidean reconstruction of *Sri Veeramakaliamman Singapore*. 14a-14b and 14c-14f show the results of our method with and without data augmentation and bundle adjustment, while 14c and 14f show the results of training with artificially injected outliers, with / without corruption of the test scene as well. Finally, the corresponding results of DPESFM [31] can be seen in 14g-14l.

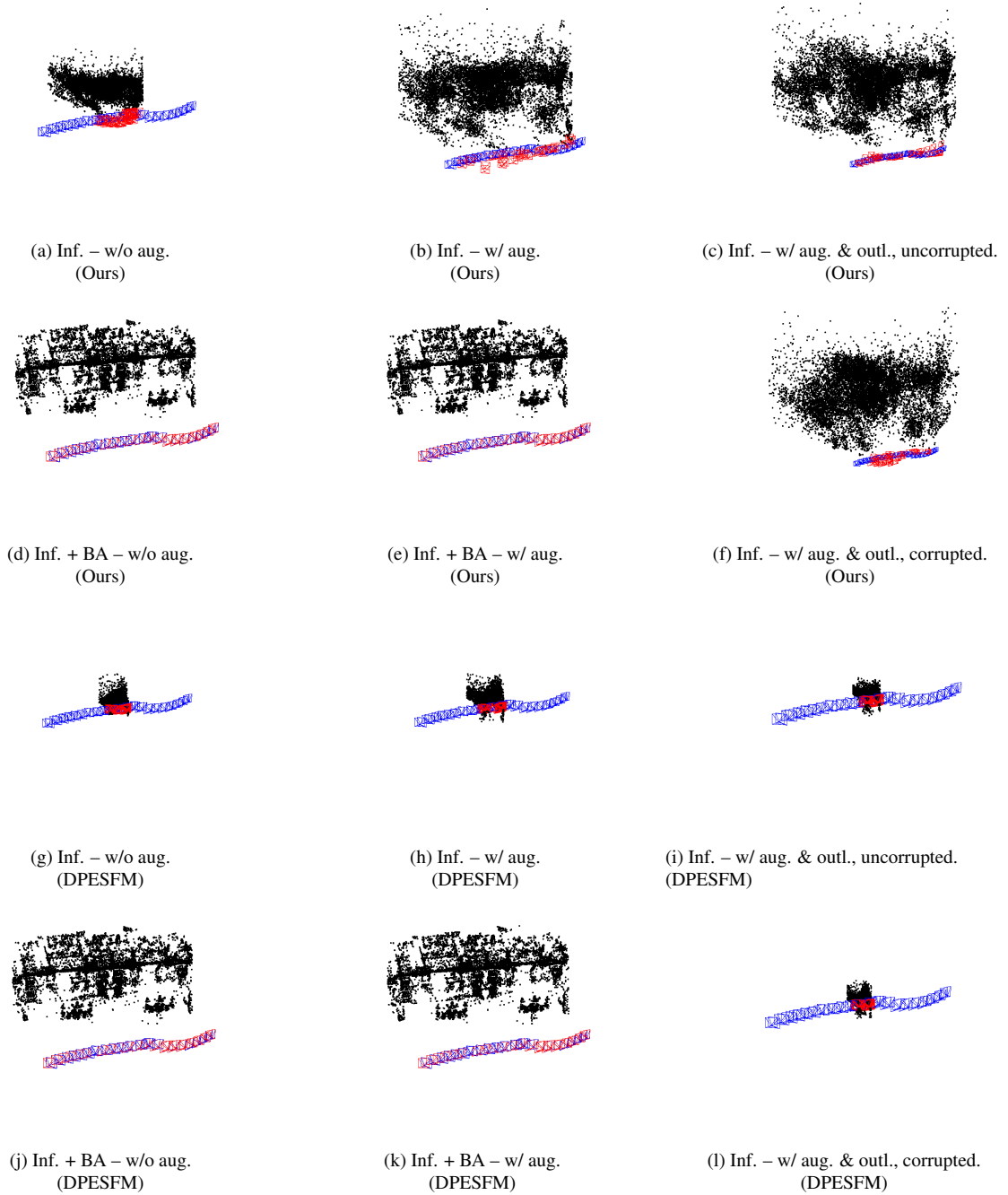


Figure 15. Euclidean reconstruction of *Yueh Hai Ching Temple Singapore*. 15a-15b and 15c-15f show the results of our method with and without data augmentation and bundle adjustment, while 15c and 15f show the results of training with artificially injected outliers, with / without corruption of the test scene as well. Finally, the corresponding results of DPESFM [31] can be seen in 15g-15l.